Omidi, Milad; St-Pierre, Luc

Mechanical Properties of Semi-Regular Lattices

Published in:
Materials & Design

DOI:
10.1016/j.matdes.2021.110324

Published: 01/01/2022

Document Version
Publisher's PDF, also known as Version of record

Please cite the original version:
Omidi, M., & St-Pierre, L. (2022). Mechanical Properties of Semi-Regular Lattices. *Materials & Design*, *213*, Article 110324. https://doi.org/10.1016/j.matdes.2021.110324

Materials & Design 213 (2022) 110324

Contents lists available at ScienceDirect

Materials & Design

journal homepage: www.elsevier.com/locate/matdes

Mechanical Properties of Semi-Regular Lattices

Milad Omidi, Luc St-Pierre *

Aalto University, Department of Mechanical Engineering, Otakaari 4, 02150 Espoo, Finland

HIGHLIGHTS

- The in-plane mechanical properties of 7 semi-regular lattices were derived analytically.
- We found a stretching-dominated topology with an elastic buckling strength 43% higher than a regular triangular lattice.
- One bending-dominated semi-regular tessellation is 85% stiffer and 11% stronger than a regular hexagonal lattice.

GRAPHICAL ABSTRACT

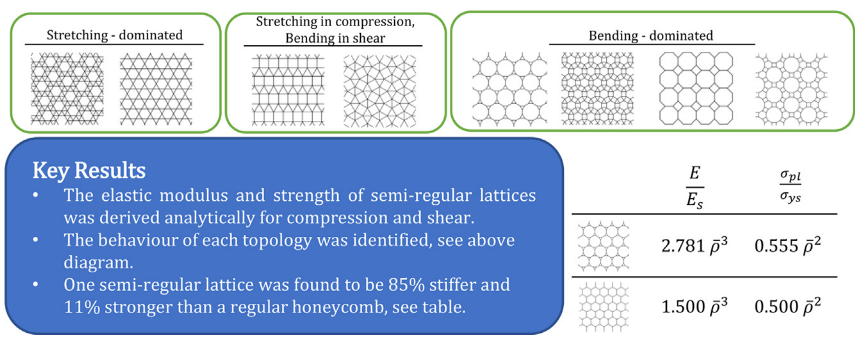

ARTICLE INFO

Article history:
Received 28 September 2021
Revised 25 November 2021
Accepted 12 December 2021
Available online 14 December 2021

Keywords:
Semi-regular tessellations
Planar lattices
Honeycombs
Cellular solids

ABSTRACT

The mechanical properties of seven semi-regular lattices were derived analytically for in-plane uniaxial compression and shear. These analytical expressions were then validated using Finite Element simulations. Our analysis showed that one topology is stretching-dominated; two are stretching-dominated in compression but bending-dominated in shear; and four are bending-dominated. To assess their potential, the properties of these seven semi-regular topologies were compared to regular lattices. We found the elastic buckling strength of the stretching-dominated semi-regular tessellation to be 43% higher than a regular triangular lattice. In addition, three of the four bending-dominated semi-regular topologies had a higher elastic modulus than a regular hexagonal lattice. In fact, one of these bending-dominated topologies was 85% stiffer and 11% stronger than a hexagonal lattice. This topology would be ideal for applications requiring a high stiffness and high energy absorption.

1. Introduction

Micro-architectured and lattice materials have a huge advantage over conventional fully-dense solids: their topology can be designed to achieve specific, and often unique, properties [1,2]. For example, architectures have been created to reach the theoretical limit on stiffness [3–5], achieve a high fracture toughness [6–8], increase energy absorption capacities [9,10], have a negative Poisson's ratio [11,12], avoid localised deformation [13,14], or have unusual elastic properties such as a ratio of bulk to shear modulus as high as 10^3 [15,16]. These lattice materials can be categorised as either spatial (3D) or planar (2D) topologies [17]. Even though spatial lattices are potentially more efficient, planar topologies have remained attractive as they are easier to manufacture on a large scale.

Planar lattices can be classified into three categories: regular, semi-regular, and other tessellations [17]. Regular lattices are made by tessellating a single regular polygon. There are only three regular tessellations [18]: hexagonal, square and triangular lattices, see Fig. 1. In contrast, semi-regular lattices are assembled by tessellating two or more regular polygons, with the same arrangement at each vertex. This arrangement generates eight semi-regular lattices [18], and these are shown in Fig. 2. Lastly,

* Corresponding author.
E-mail address: luc.st-pierre@aalto.fi (L. St-Pierre).

https://doi.org/10.1016/j.matdes.2021.110324
0264-1275/© 2021 The Author(s). Published by Elsevier Ltd.

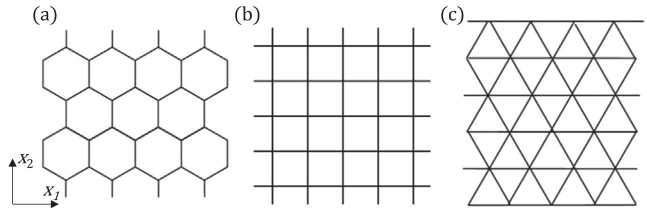

Fig. 1. The three regular tessellations: (a) hexagonal, (b) square, and (c) triangular lattices.

other lattices can be created using one or more polygons (regular or irregular) and/or by changing the nodal connectivity (defined as the number of bars meeting at each joint).

The mechanical behaviour of any lattice can be categorised in two groups: bending- or stretching-dominated [19]. Stretching-dominated lattices are significantly stiffer and stronger than bending-dominated topologies; however, the latter offer superior energy absorption capacities. A key parameter to determine if a lattice is bending- or stretching-dominated is the nodal connectivity [20]. Planar lattices with a nodal connectivity $Z \leqslant 3$, such as the hexagonal lattice (Fig. 1a), are bending-dominated. Otherwise, topologies with $Z \geqslant 6$, like the triangular lattice (Fig. 1c), are stretching-dominated. Finally, lattices with $Z = 4$ or 5 can be either bending- or stretching-dominated. For example, a square lattice (Fig. 1b) has a nodal connectivity $Z = 4$ and it is stretching-dominated when loading is aligned with the struts, but bending-dominated otherwise.

The mechanical properties of all three regular lattices have been studied extensively [21–27]. Analytical expressions for the modulus and strength of regular lattices were first derived by [21–23], followed by in-depth analyses of their elastic buckling strength [25] and tensile elastoplastic response [26]. These analytical studies were then corroborated by experiments performed on hexagonal [21], square [24], and triangular lattices [27].

Semi-regular tessellations, however, have received considerably less attention; the trihexagonal lattice (also referred to as kagome, see Fig. 2a) is the only topology to have been studied extensively. This architecture has impressive properties: it is stretching-dominated and as stiff and strong as the triangular lattice despite having a lower nodal connectivity [28,17]. In addition, the trihexagonal lattice has a remarkably high fracture toughness [29] and a great potential for actuation [30,31]. Reports on other semi-regular topologies are scarce: the stiffness and strength of the snub-square lattice were reported by Their and St-Pierre [32]; whereas the elastic and shear moduli of the snub-trihexagonal and rhombi-trihexagonal were obtained numerically by Elsayed and Pasini [33] and Pronk et al. [34], respectively. At the moment, it is impossible to evaluate the potential of most semi-regular tessellations since many of their mechanical properties remain unknown. Therefore, the aim of this study is to provide all missing properties for semi-regular lattices and compare their performances to those of regular topologies.

This article is structured as follows. Analytical equations for the elastic modulus, compressive strength, as well as shear modulus and strength, are derived in Section 2. These analytical expressions are validated using Finite Element (FE) simulations, and a description of the modelling approach is given in Section 3. A comparison between analytical and numerical results is presented in Section 4 along with a discussion on the potential of semi-regular lattices.

2. Analytical modelling

In this section, the modulus and strength of all semi-regular lattices are derived analytically for in-plane uniaxial compression and shear. Only the trihexagonal lattice (Fig. 2a) is excluded from this analysis since its properties are already available in the literature [28,23,17]. Here, we assume that all lattices are made from an isotropic linear elastic, perfectly plastic solid, characterized by a Young's modulus E_s and a yield strength σ_{ys}. All cell walls are considered to have a thickness t, a length ℓ, and an out-of-plane depth b. The cell walls are considered to behave (i) as pin-jointed trusses in the case of stretching-dominated lattices or (ii) as Euler-Bernoulli beams for bending-dominated topologies. Two failure modes are considered when predicting the strength of a lattice: plastic collapse/yielding and elastic buckling. Bending-dominated topologies fail by plastic collapse when the maximum bending moment in a cell wall reaches the fully plastic moment:

$$M_p = \frac{bt^2\sigma_{ys}}{4}. \tag{1}$$

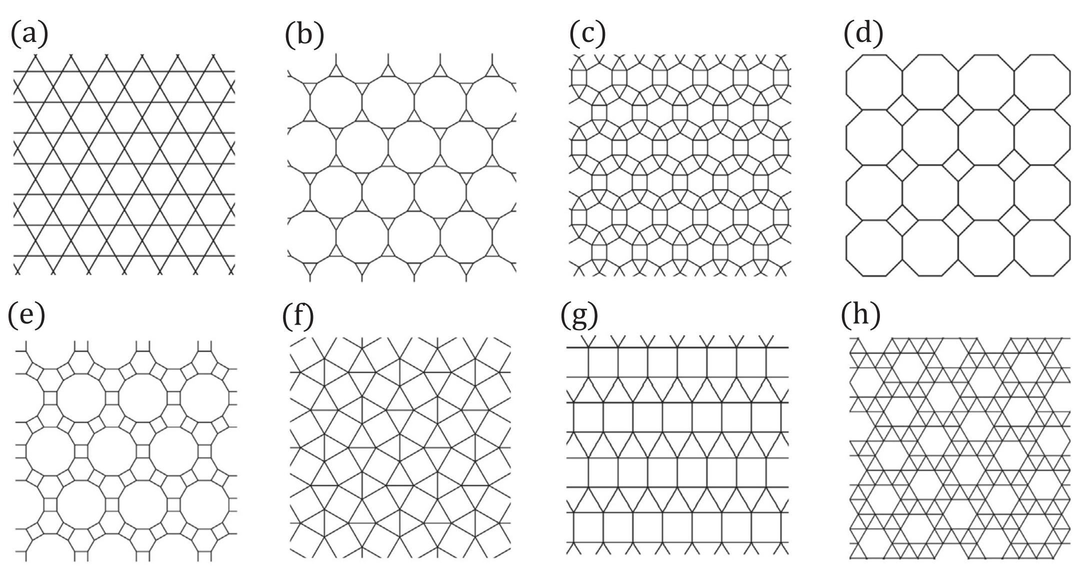

Fig. 2. The eight semi-regular tessellations: (a) trihexagonal (or kagome), (b) truncated-hexagonal, (c) rhombi-trihexagonal, (d) truncated-square, (e) truncated-trihexagonal, (f) snub-square, (g) elongated-triangular, and (h) snub-trihexagonal lattices. The nomenclature is based on Williams [18].

Otherwise, stretching-dominated lattices fail by yielding when the axial stress in a cell wall (in tension or compression) reaches the yield strength σ_{ys} of the parent material. In contrast, elastic buckling occurs when the axial compressive force in a cell wall reaches the Euler buckling load [35]:

$$T_{cr} = \frac{n^2\pi^2 E_s I}{\ell^2}, \tag{2}$$

where $I = bt^3/12$ is the second moment of area and n is the end constraint factor. The operative failure mode is the one associated with the lowest load. Note that these assumptions are identical to those used in previous studies [21,28,23,17], which will enable a fair comparison between our results and the properties of regular lattices.

Our analysis of bending-dominated lattices will rely heavily on the stiffness matrix of a single beam. Consider a beam of length ℓ subjected to a transverse displacement Δ, and rotations θ_i and θ_j at ends i and j, respectively, see Fig. 3. These rotations and displacement will give rise to a transverse force V_{ij}, and bending moments M_{ij} and M_{ji} at ends i and j, respectively. These quantities are related by [36]:

$$\begin{Bmatrix} M_{ij} \\ M_{ji} \\ V_{ij} \end{Bmatrix} = \frac{E_s I}{\ell}\begin{bmatrix} 4 & 2 & 6/\ell \\ 2 & 4 & 6/\ell \\ 6/\ell & 6/\ell & 12/\ell^2 \end{bmatrix}\begin{Bmatrix} \theta_i \\ \theta_j \\ \Delta_{ij} \end{Bmatrix}. \tag{3}$$

This equation can be used to model the deformation of lattices as follows. First, the bending moments and transverse force for each bar can be expressed using Eq. (3). Second, equilibrium conditions at each vertex, and the boundary conditions, are used to form a system of equations from which the deflections and rotations can be solved. This procedure is demonstrated next.

2.1. Truncated-hexagonal lattice

The truncated-hexagonal tessellation has two dodecagons and a triangle meeting at each vertex, see Fig. 4. It has a nodal connectivity $Z = 3$ and therefore, its behaviour is bending-dominated [20]. This topology has 6-fold rotational symmetry and consequently, its in-plane elastic properties are isotropic [37]. The relative density of the truncated-hexagonal lattice is given by:

$$\bar{\rho} = \frac{6\sqrt{3}}{(2+\sqrt{3})^2}\left(\frac{t}{\ell}\right) = 0.746\left(\frac{t}{\ell}\right). \tag{4}$$

2.1.1. Compression

Consider the truncated-hexagonal lattice subjected to a uniaxial compressive stress σ in x_2, see Fig. 4a. A representative unit cell is shown in Fig. 4a, where the nominal stress σ is replaced by an equivalent force:

$$F = (2+\sqrt{3})\sigma b\ell. \tag{5}$$

In compression, the truncated-hexagonal lattice deforms primarily by bending bar bb. This strut will have a transverse deflection Δ and a rotation θ at both ends, see Fig. 4a. The component of F perpendicular to bar bb corresponds to the transverse force V_{bb}, which can also be expressed as a function of Δ and θ using the stiffness matrix introduced in Eq. (3). This gives:

$$V_{bb} = \frac{12E_s I}{\ell^2}\left(\frac{\Delta}{\ell} - \theta\right) = \frac{\sqrt{3}}{4}F. \tag{6}$$

In addition, equilibrium of moments at b requires that:

$$M_{ba} + M_{bb'} + M_{bb} = \frac{6E_s I}{\ell}\left(\frac{\Delta}{\ell} - 2\theta\right) = 0. \tag{7}$$

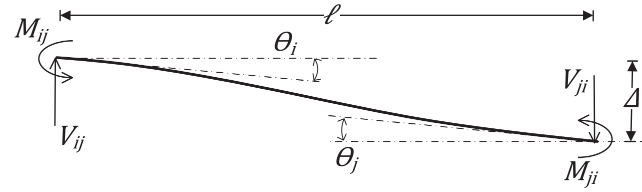

Fig. 3. Deformation and reaction loads for a beam in bending. The end rotations θ_i and θ_j and the deflection Δ create the bending moments M_{ij} and M_{ji}, and a transverse force $V_{ij} = V_{ji}$.

Again, these moments were obtained using the stiffness matrix given in Eq. (3). Eqs. (6) and (7) can be used to solve for Δ and θ, which gives:

$$\Delta = \frac{\sqrt{3}}{24}\frac{F\ell^3}{E_s I}, \tag{8}$$

$$\theta = \frac{\sqrt{3}}{48}\frac{F\ell^2}{E_s I}. \tag{9}$$

The component of Δ along x_2 is used to compute the compressive strain:

$$\varepsilon_2 = \frac{\sqrt{3}/2\cdot\Delta}{(3/2+\sqrt{3})\ell} = \frac{\sqrt{3}}{2}\frac{\sigma}{E_s}\left(\frac{\ell}{t}\right)^3. \tag{10}$$

The elastic modulus of the lattice is $E = \sigma/\varepsilon_2$, which returns:

$$\frac{E}{E_s} = \frac{2}{\sqrt{3}}\left(\frac{t}{\ell}\right)^3 = 2.780\bar{\rho}^3. \tag{11}$$

Otherwise, the component of Δ in x_1 gives a deformation:

$$\varepsilon_1 = -\frac{\Delta}{(2+\sqrt{3})\ell} = -\frac{\sqrt{3}}{2}\frac{\sigma}{E_s}\left(\frac{\ell}{t}\right)^3, \tag{12}$$

and therefore the Poisson's ratio is:

$$\nu = -\frac{\varepsilon_1}{\varepsilon_2} = 1. \tag{13}$$

Next, we turn our attention to the compressive strength of the truncated-hexagonal lattice. This topology is bending-dominated and the maximum bending moment in a cell wall is:

$$M_{bb} = \frac{\sqrt{3}}{8}F\ell = \frac{(3+2\sqrt{3})}{8}\sigma b\ell^2. \tag{14}$$

Equating this to the fully plastic moment (Eq. (1)) gives the plastic collapse strength of the lattice:

$$\frac{(\sigma_{pl})_2}{\sigma_{ys}} = \frac{2}{(3+2\sqrt{3})}\left(\frac{t}{\ell}\right)^2 = 0.556\bar{\rho}^2. \tag{15}$$

Otherwise, bar aa is loaded in compression and may buckle elastically. The axial force in this bar is $N_{aa} = F$, and equating this to the Euler buckling load (Eq. (2)) returns the elastic buckling strength of a truncated-hexagonal lattice:

$$\frac{(\sigma_{el})_2}{E_s} = \frac{n^2\pi^2}{12(2+\sqrt{3})}\left(\frac{t}{\ell}\right)^3 = 0.082\bar{\rho}^3, \tag{16}$$

where the end constraint factor $n = 0.394$ is derived analytically in Appendix A.1. The same procedure can be followed to derive the compressive strength in x_1. This analysis is not detailed here for the sake of brevity, but it leads to $(\sigma_{pl})_1 = (\sigma_{pl})_2$. Note that elastic buckling does not occur for uniaxial compression in x_1.

2.1.2. Shear

Consider the truncated-hexagonal lattice loaded in pure in-plane shear as shown in Fig. 4b. A representative unit cell in

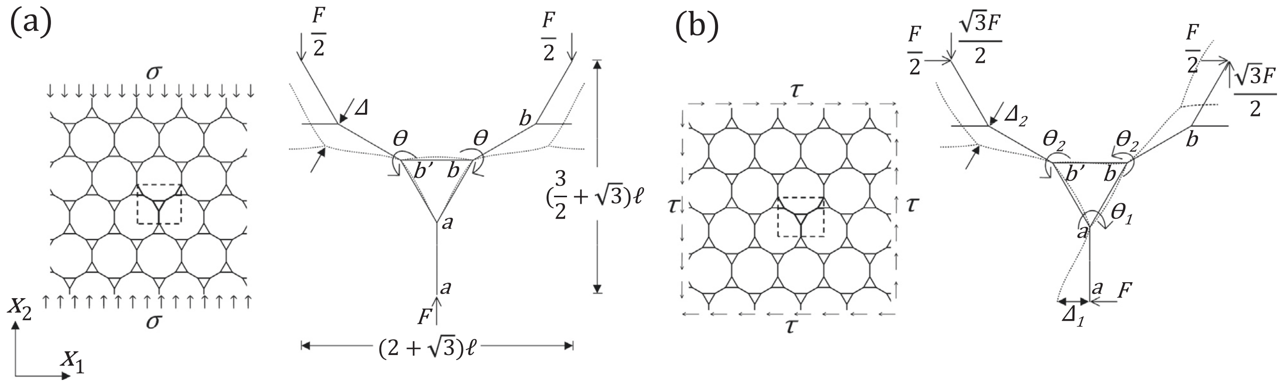

Fig. 4. Deformation of a truncated-hexagonal lattice under (a) compression and (b) shear.

included in Fig. 4b, where the nominal shear stress τ is replaced by an equivalent force:

$$F = (2+\sqrt{3})\,\tau b\ell. \tag{17}$$

In shear, the truncated-hexagonal lattice deforms by bending bars *aa* and *bb*. Their deformation is characterised by four parameters: the transverse deflections Δ_1 and Δ_2, and rotations θ_1 and θ_2, see Fig. 4b. Using the stiffness matrix in Eq. (3), the transverse force in bar *aa* can be expressed as:

$$V_{aa} = \frac{12E_sI}{\ell^2}\left(\frac{\Delta_1}{\ell} - \theta_1\right) = F, \tag{18}$$

and, similarly, the transverse force in bar *bb* is given by:

$$V_{bb} = \frac{12E_sI}{\ell^2}\left(\theta_2 - \frac{\Delta_2}{\ell}\right) = -\frac{F}{2}. \tag{19}$$

Moreover, equilibrium of moments at vertex a gives:

$$M_{aa} + M_{ab} + M_{ab\prime} = \frac{2E_sI}{\ell}\left(\frac{3\Delta_1}{\ell} - 7\theta_1 + 2\theta_2\right) = 0, \tag{20}$$

and for vertex b:

$$M_{ba} + M_{bb\prime} + M_{bb} = \frac{2E_sI}{\ell}\left(8\theta_2 - \frac{3\Delta_2}{\ell} - \theta_1\right) = 0. \tag{21}$$

The four unknown displacements can be solved using Eqs. (18)–(21), which gives:

$$\theta_1 = \frac{F\ell^2}{12E_sI}, \tag{22}$$

$$\Delta_1 = \frac{F\ell^3}{6E_sI}, \tag{23}$$

$$\theta_2 = \frac{F\ell^2}{24E_sI}, \tag{24}$$

$$\Delta_2 = \frac{F\ell^3}{12E_sI}. \tag{25}$$

Next, the nominal shear strain can be expressed as:

$$\gamma = \frac{2(\Delta_1+\Delta_2)}{(3+2\sqrt{3})\ell} = \frac{6}{\sqrt{3}}\frac{\tau}{E_s}\left(\frac{\ell}{t}\right)^3, \tag{26}$$

and the shear modulus $G = \tau/\gamma$ is:

$$\frac{G}{E_s} = \frac{\sqrt{3}}{6}\left(\frac{t}{\ell}\right)^3 = 0.695\,\bar{\rho}^3. \tag{27}$$

This result respects the relationship $G = E/(2(1+\nu))$ characteristic of isotropic materials (see Eq. (11) and (13) for E and ν, respectively).

The truncated-hexagonal lattice fails by plastic collapse in shear. The maximum bending moment is located at the ends of bar *aa* and is:

$$M_{aa} = \frac{F\ell}{2} = \frac{(2+\sqrt{3})}{2}\tau b\ell^2. \tag{28}$$

Setting M_{aa} equal to the fully plastic moment (Eq. (1)) returns the shear strength:

$$\frac{\tau_{pl}}{\sigma_{ys}} = \frac{1}{2(2+\sqrt{3})}\left(\frac{t}{\ell}\right)^2 = 0.241\,\bar{\rho}^2. \tag{29}$$

2.2. Rhombi-trihexagonal lattice

The rhombi-trihexagonal lattice has a triangle, two squares, and a hexagon meeting at each vertex, see Fig. 5. The bars forming the squares are anticipated to bend when subjected to compression or shear and therefore, the lattice is expected to be bending-dominated despite its nodal connectivity $Z = 4$. This pattern has a 6-fold rotational symmetry and consequently, it is in-plane elastically isotropic [37]. Its relative density is given by:

$$\bar{\rho} = 4(2\sqrt{3}-3)\left(\frac{t}{l}\right) = 1.856\left(\frac{t}{l}\right). \tag{30}$$

2.2.1. Compression

Consider the rhombi-trihexagonal lattice subjected to an in-plane compressive stress σ in the x_2 direction, see Fig. 5a. The unit cell, given in Fig. 5a, includes an equivalent force F, which is related to the compressive stress σ by:

$$F = \frac{(1+\sqrt{3})}{2}\sigma b\ell. \tag{31}$$

In compression, the lattice is expected to deform by bending bars *ac* and *bd*. Rotations at vertices b and $b\prime$ are equal (but in opposite directions) due to symmetry, and there are no rotations at a, see Fig. 5a. Using Eq. (3), the transverse force in bars *ac* and *bd* can be written as a function of the displacement field, which gives:

$$V_{ac} = V_{bd} = \frac{6E_sI}{\ell^2}\left(\frac{2\Delta}{\ell} - \theta\right) = \frac{\sqrt{3}}{4}F. \tag{32}$$

Otherwise, the sum of moments at vertex b should be zero, and this gives:

$$M_{ba} + M_{bb\prime} + M_{bd} + M_{be} = \frac{6E_sI}{\ell}\left(\frac{\Delta}{\ell} - 2\theta\right) = 0. \tag{33}$$

Using Eq. (32) and (33) to solve for Δ and θ returns:

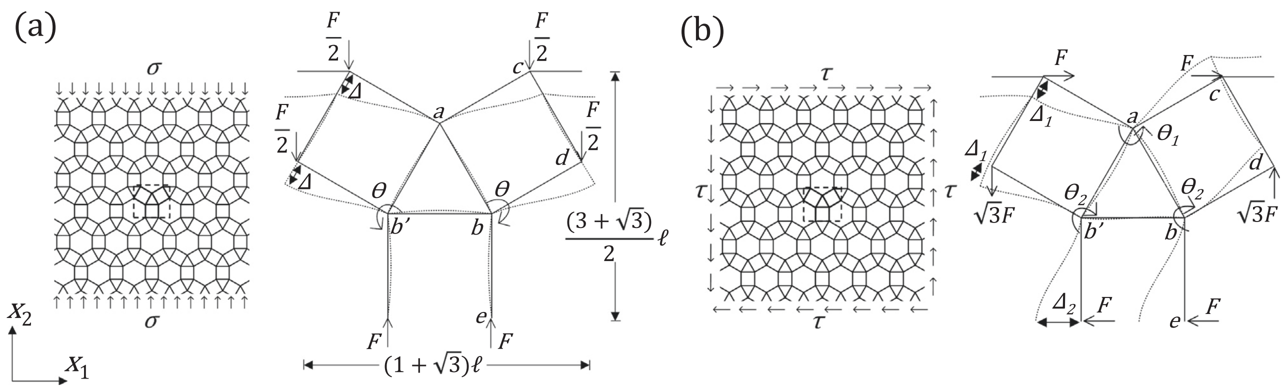

Fig. 5. Deformation of a rhombi-trihexagonal lattice under (a) compression and (b) shear.

$$\theta = \frac{\sqrt{3}}{72}\frac{F\ell^2}{E_sI}, \tag{34}$$

$$\Delta = \frac{\sqrt{3}}{36}\frac{F\ell^3}{E_sI}. \tag{35}$$

The compressive strain is calculated with the component of Δ in the x_2 direction, which gives:

$$\varepsilon_2 = \frac{\sqrt{3}/2\cdot\Delta}{(3+\sqrt{3})\ell/2} = \frac{\sqrt{3}}{6}\frac{\sigma}{E_s}\left(\frac{\ell}{t}\right)^3, \tag{36}$$

and the elastic modulus $E = \sigma/\varepsilon_2$ becomes:

$$\frac{E}{E_s} = 2\sqrt{3}\left(\frac{t}{\ell}\right)^3 = 0.542\bar{\rho}^3. \tag{37}$$

In addition, the strain in x_1 direction is:

$$\varepsilon_1 = \frac{-\Delta}{(1+\sqrt{3})\ell} = -\frac{\sqrt{3}}{6}\frac{\sigma}{E_s}\left(\frac{\ell}{t}\right)^3, \tag{38}$$

and therefore, the Poisson's ratio is:

$$\nu = -\frac{\varepsilon_1}{\varepsilon_2} = 1. \tag{39}$$

The rhombi-trihexagonal lattice is bending-dominated and the maximum bending moment is:

$$M_{ac} = M_{db} = \frac{5\sqrt{3}}{36}F\ell = \frac{5(3+\sqrt{3})}{72}\sigma b\ell^2. \tag{40}$$

Equating this to the fully plastic moment (Eq. (1)) returns the plastic collapse strength of the lattice:

$$\frac{(\sigma_{pl})_2}{\sigma_{ys}} = \frac{18}{5(3+\sqrt{3})}\left(\frac{t}{\ell}\right)^2 = 0.221\bar{\rho}^2. \tag{41}$$

This topology may also fail by elastic buckling of bar *be*. The axial compressive force in this bar is $N_{be} = F$, and equating this to the Euler buckling load (Eq. (2)) gives us the elastic buckling strength:

$$\frac{(\sigma_{el})_2}{E_s} = \frac{n^2\pi^2}{6(1+\sqrt{3})}\left(\frac{t}{\ell}\right)^3 = 0.071\bar{\rho}^3, \tag{42}$$

where the end constraint factor $n = 0.871$ is obtained in Appendix A.2. Finally, note that when the rhombi-trihexagonal lattice is compressed in the x_1 direction, plastic collapse is the only failure mode and we find $(\sigma_{pl})_1 = (\sigma_{pl})_2$.

2.2.2. Shear

The rhombi-trihexagonal lattice subjected to pure shear is shown in Fig. 5b along with its unit cell, where the nominal shear stress τ has been replaced by an equivalent shear force F given by:

$$F = \frac{(1+\sqrt{3})}{2}\tau b\ell. \tag{43}$$

The deformation of the lattice in shear is characterised by four variables: two deflections, Δ_1 and Δ_2, and two rotations, θ_1 and θ_2, see Fig. 5b. Using Eq. (3), the transverse force in bar *be* can be expressed as:

$$V_{be} = \frac{12E_sI}{\ell^2}\left(\frac{\Delta_2}{\ell} - \theta_2\right) = F, \tag{44}$$

whereas that in bar *ac* (or *bd*) is:

$$V_{ac} = V_{bd} = \frac{6E_sI}{\ell^2}\left(\theta_1 - \theta_2 - \frac{2\Delta_1}{\ell}\right) = -\frac{F}{2}. \tag{45}$$

Also, equilibrium of moments at vertex *a* returns:

$$2(M_{ac} + M_{ab}) = \frac{4E_sI}{\ell}\left(4\theta_1 - \frac{3\Delta_1}{\ell} - 2\theta_2\right) = 0, \tag{46}$$

and at vertex *b* gives:

$$M_{ba} + M_{bb'} + M_{bd} + M_{be} = \frac{2E_sI}{\ell}\left(2\theta_1 - \frac{3\Delta_1}{\ell} - 10\theta_2 + \frac{3\Delta_2}{\ell}\right) = 0. \tag{47}$$

The displacement field can be solved with Eqs. (44)–(47), and this yields:

$$\theta_1 = \frac{F\ell^2}{18E_sI}, \tag{48}$$

$$\Delta_1 = \frac{F\ell^3}{18E_sI}, \tag{49}$$

$$\theta_2 = \frac{F\ell^2}{36E_sI}, \tag{50}$$

$$\Delta_2 = \frac{F\ell^3}{9E_sI}. \tag{51}$$

Next, we can write the shear strain:

$$\gamma = \frac{4\Delta_1 + \Delta_2}{(3+\sqrt{3})\ell} = \frac{2\sqrt{3}}{3}\frac{\tau}{E_s}\left(\frac{\ell}{t}\right)^3, \tag{52}$$

and the shear modulus $G = \tau/\gamma$ becomes:

$$\frac{G}{E_s} = \frac{\sqrt{3}}{2}\left(\frac{t}{\ell}\right)^3 = 0.135\bar{\rho}^3. \tag{53}$$

The rhombi-trihexagonal lattice is in-plane isotropic and consequently, $G = E/(2(1+\nu))$.

This lattice is bending-dominated in shear and the maximum bending moment in a cell wall is:

$$M_{be} = \frac{F\ell}{2} = \frac{(1+\sqrt{3})}{4}\tau b\ell^2. \tag{54}$$

Setting this equal to the fully plastic moment (Eq. (1)), returns the plastic collapse strength:

$$\frac{\tau_{pl}}{\sigma_{ys}} = \frac{1}{(1+\sqrt{3})}\left(\frac{t}{\ell}\right)^2 = 0.106\bar{\rho}^2. \tag{55}$$

2.3. Truncated-square lattice

The truncated-square lattice, shown in Fig. 6, has a square and two octagons meeting at each vertex. It has a nodal connectivity $Z = 3$ and consequently, its behaviour is bending-dominated [20]. This tessellation has a 4-fold rotational symmetry, and therefore, its elastic properties are not isotropic [37]. Its relative density is given by:

$$\bar{\rho} = \frac{6}{(1+\sqrt{2})^2}\left(\frac{t}{\ell}\right) = 1.029\left(\frac{t}{\ell}\right). \tag{56}$$

2.3.1. Compression

The deformation of a truncated-square lattice in compression can be analysed with the unit cell shown in Fig. 6a, where the nominal compressive stress σ is replaced by an equivalent force:

$$F = (1+\sqrt{2})\sigma b\ell. \tag{57}$$

This tessellation deforms by bending bar *ab*. This strut has a transverse deflection Δ, but rotations are prevented at both extremities due to symmetry. Therefore, the transverse force in beam *ab* is:

$$V_{ab} = \frac{12E_sI}{\ell^3}\Delta = \frac{\sqrt{2}F}{4}, \tag{58}$$

from which it is straightforward to find the deflection:

$$\Delta = \frac{\sqrt{2}}{48}\frac{F\ell^3}{E_sI}. \tag{59}$$

Next, the compressive strain is:

$$\varepsilon_2 = \frac{\sqrt{2}\Delta}{(1+\sqrt{2})\ell} = \frac{1}{2}\frac{\sigma}{E_s}\left(\frac{\ell}{t}\right)^3, \tag{60}$$

and the elastic modulus becomes:

$$\frac{E_2}{E_s} = 2\left(\frac{t}{\ell}\right)^3 = 1.833\bar{\rho}^3, \tag{61}$$

where the subscript 2 is used to emphasise that elastic properties are not isotropic for this topology. Otherwise, the strain in x_1 is:

$$\varepsilon_1 = -\frac{\sqrt{2}\Delta}{(1+\sqrt{2})\ell} = -\frac{1}{2}\frac{\sigma}{E_s}\left(\frac{\ell}{t}\right)^3, \tag{62}$$

and the Poisson's ratio is:

$$\nu_{12} = -\frac{\varepsilon_1}{\varepsilon_2} = 1. \tag{63}$$

The maximum bending moment in a truncated-square lattice is:

$$M_{ab} = \frac{\sqrt{2}}{8}F\ell = \frac{(2+\sqrt{2})}{8}\sigma b\ell^2, \tag{64}$$

and equating this to the fully plastic moment (Eq. (1)) returns the plastic collapse strength:

$$\frac{(\sigma_{pl})_2}{\sigma_{ys}} = (2-\sqrt{2})\left(\frac{t}{\ell}\right)^2 = 0.553\bar{\rho}^2. \tag{65}$$

A truncated-square lattice can also fail by elastic buckling of bar *aa*. The axial compressive force in this strut is $N_{aa} = F$, and setting this equal to the Euler buckling load (Eq. (2)) yields the elastic buckling strength:

$$\frac{(\sigma_{el})_2}{E_s} = \frac{n^2\pi^2}{12(1+\sqrt{2})}\left(\frac{t}{\ell}\right)^3 = 0.168\bar{\rho}^3, \tag{66}$$

where the end constraint factor $n = 0.734$ is derived in Appendix A.3. Finally, note that all properties are the same for compression in x_1 because of the 4-fold rotational symmetry of the truncated-square lattice.

2.3.2. Shear

Consider the truncated-square lattice subjected to pure shear. The deformation of its unit cell is given in Fig. 6b, where the nominal shear stress τ has been replaced by an equivalent force:

$$F = (1+\sqrt{2})\tau b\ell. \tag{67}$$

In shear, the truncated-square lattice deforms by bending the vertical and horizontal bars, and the displacement field is characterised by their transverse deflection Δ and rotation θ. The transverse force in bar *aa* is:

$$V_{aa} = \frac{12E_sI}{\ell^2}\left(\frac{\Delta}{\ell} - \theta\right) = F, \tag{68}$$

and equilibrium of moments at vertex *a* gives:

$$M_{aa} + 2M_{ab} = \frac{2E_sI}{\ell}\left(\frac{3\Delta}{\ell} - 5\theta\right) = 0. \tag{69}$$

Using the last two equations to find Δ and θ returns:

$$\theta = \frac{F\ell^2}{8E_sI}, \tag{70}$$

$$\Delta = \frac{5}{24}\frac{F\ell^3}{E_sI}. \tag{71}$$

Next, the shear strain can be expressed as:

$$\gamma = \frac{2\Delta}{(1+\sqrt{2})\ell} = 5\frac{\tau}{E_s}\left(\frac{\ell}{t}\right)^3, \tag{72}$$

and the shear modulus $G_{12} = \tau/\gamma$ becomes:

$$\frac{G_{12}}{E_s} = \frac{1}{5}\left(\frac{t}{\ell}\right)^3 = 0.183\bar{\rho}^3. \tag{73}$$

Otherwise, the maximum bending moment in a truncated-square lattice is at vertex *b* and is given by:

$$M_{bb} = \frac{F\ell}{2} = \frac{(1+\sqrt{2})\tau b\ell^2}{2}. \tag{74}$$

Equating this to the fully plastic moment (Eq. (1)) gives us the plastic collapse strength in shear:

$$\frac{\tau_{pl}}{\sigma_{ys}} = \frac{(\sqrt{2}-1)}{2}\left(\frac{t}{\ell}\right)^2 = 0.195\bar{\rho}^2. \tag{75}$$

2.4. Truncated-trihexagonal lattice

The truncated-trihexagonal lattice has a square, a hexagon and a dodecagon meeting at each vertex, see Fig. 7. Its behaviour is bending-dominated, since it has a nodal connectivity $Z = 3$ [20]. This topology has a 6-fold rotational symmetry; therefore, its in-plane elastic properties are isotropic. Its relative density is given by:

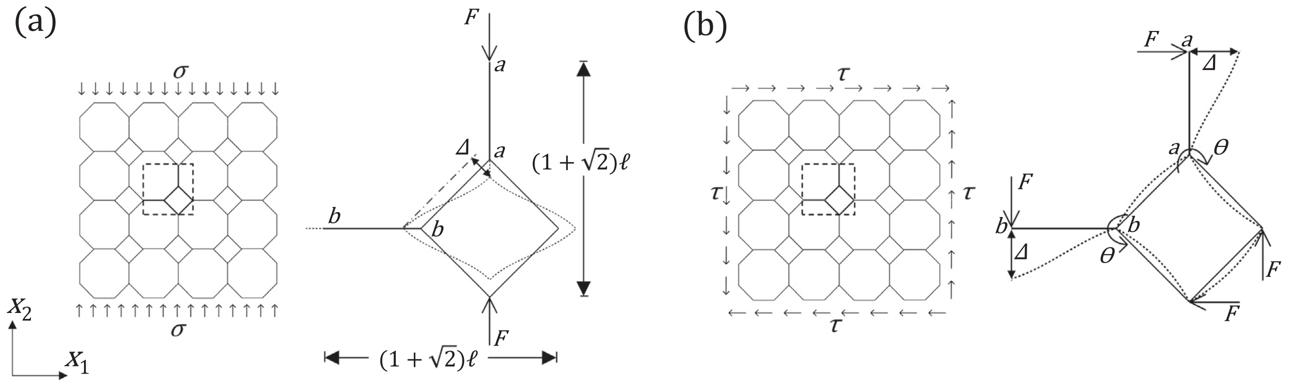

Fig. 6. Deformation of a truncated-square lattice under (a) compression and (b) shear.

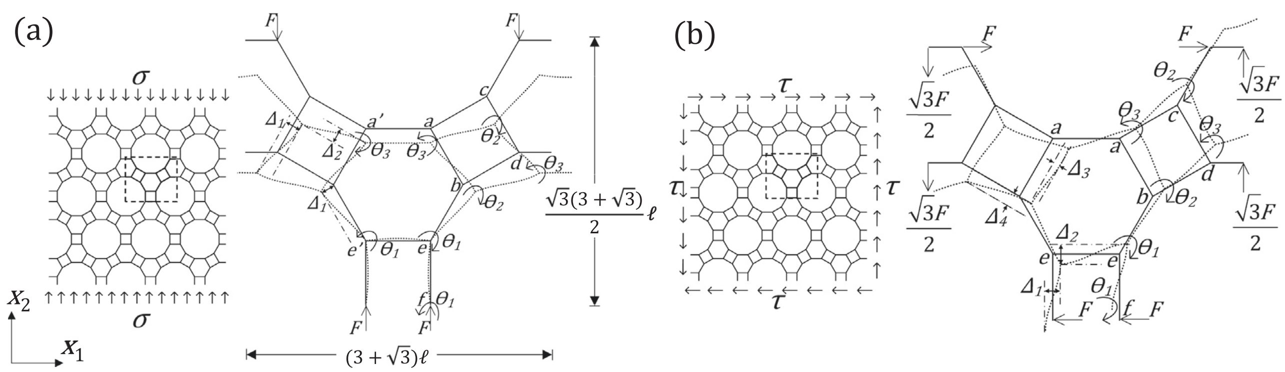

Fig. 7. Deformation of a truncated-trihexagonal lattice under (a) compression and (b) shear.

$$\bar{\rho} = \frac{4\sqrt{3}}{(1+\sqrt{3})^2}\left(\frac{t}{\ell}\right) = 0.928\left(\frac{t}{\ell}\right). \tag{76}$$

2.4.1. Compression

When a truncated-trihexagonal lattice is loaded in compression, the deformation of its unit cell is characterised by two displacements (Δ_1, Δ_2) and three rotations $(\theta_1, \theta_2, \theta_3)$, see Fig. 7a. Here, the compressive stress σ is replaced by an equivalent force:

$$F = \frac{(3+\sqrt{3})}{2}\sigma b \ell. \tag{77}$$

Bars *ac* and *bd* experience the same transverse force, which is given by:

$$V_{ac} = V_{bd} = \frac{6E_sI}{\ell^2}\left(\theta_3 - \theta_2 + \frac{2\Delta_2}{\ell}\right) = \frac{\sqrt{3}}{4}F. \tag{78}$$

Next, equilibrium of forces, in the x_2 direction, at vertex *b* gives:

$$V_{be} - V_{ab} = \sqrt{3}V_{bd} \Rightarrow \frac{6E_sI}{\ell^2}\left(\frac{4\Delta_1}{\ell} - \theta_1 - \theta_3\right) = \frac{3}{4}F. \tag{79}$$

Finally, equilibrium of moments at vertices a, b and e yields:

$$M_{aa'} + M_{ac} + M_{ab} = \tfrac{2E_sI}{\ell}\left(5\theta_3 - 2\theta_2 + \tfrac{3(\Delta_2 - \Delta_1)}{\ell}\right) = 0, \tag{80}$$

$$M_{ba} + M_{bd} + M_{be} = \tfrac{2E_sI}{\ell}\left(2\theta_3 - 6\theta_2 - \theta_1 + \tfrac{3\Delta_2}{\ell}\right) = 0, \tag{81}$$

$$M_{ef} + M_{ee'} + M_{eb} = \tfrac{2E_sI}{\ell}\left(\tfrac{3\Delta_1}{\ell} - 4\theta_1 - \theta_2\right) = 0, \tag{82}$$

respectively. Solving the displacement field using Eqs. (78)–(82) returns:

$$\theta_1 = \frac{(30 - 7\sqrt{3})}{744}\frac{F\ell^2}{E_sI}, \tag{83}$$

$$\theta_2 = \frac{(10\sqrt{3} - 3)}{744}\frac{F\ell^2}{E_sI}, \tag{84}$$

$$\theta_3 = \frac{(33 - 17\sqrt{3})}{744}\frac{F\ell^2}{E_sI}, \tag{85}$$

$$\Delta_1 = \frac{(13 - 2\sqrt{3})}{248}\frac{F\ell^3}{E_sI}, \tag{86}$$

$$\Delta_2 = \frac{(29\sqrt{3} - 18)}{744}\frac{F\ell^3}{E_sI}. \tag{87}$$

The vertical components of Δ_1 and Δ_2 are used to compute the compressive strain:

$$\varepsilon_2 = \frac{3\Delta_1 + \sqrt{3}\Delta_2}{(3+3\sqrt{3})\ell} = \frac{2(21+4\sqrt{3})}{31(1+\sqrt{3})}\frac{\sigma}{E_s}\left(\frac{\ell}{t}\right)^3, \tag{88}$$

and the elastic modulus becomes:

$$\frac{E}{E_s} = \frac{31(1+\sqrt{3})}{2(21+4\sqrt{3})}\left(\frac{t}{\ell}\right)^3 = 1.896\bar{\rho}^3. \tag{89}$$

Moreover, the strain in the x_1 direction is:

$$\varepsilon_1 = -\frac{\sqrt{3}\Delta_1 + \Delta_2}{(3+\sqrt{3})\ell} = -\frac{2(21+4\sqrt{3})}{31(1+\sqrt{3})}\frac{\sigma}{E_s}\left(\frac{\ell}{t}\right)^3, \tag{90}$$

and therefore the Poisson's ratio is:

$$\nu = -\frac{\varepsilon_1}{\varepsilon_2} = 1. \tag{91}$$

Next, we turn our attention to the compressive strength of the lattice. The maximum bending moment is:

$$M_{ba} = \frac{(19\sqrt{3}+78)}{372}F\ell, \tag{92}$$

and equating this to the fully plastic moment (Eq. (1)) gives us the plastic collapse strength:

$$\frac{(\sigma_{pl})_2}{\sigma_{ys}} = \frac{62}{(97+45\sqrt{3})}\left(\frac{t}{\ell}\right)^2 = 0.411\,\bar{\rho}^2. \tag{93}$$

A truncated-trihexagonal lattice can also fail by elastic buckling of bar *ef*. The axial compressive force in this bar is $N_{ef} = F$ and setting equal to the Euler buckling load (Eq. (2)) returns the elastic buckling strength:

$$\frac{(\sigma_{el})_2}{E_s} = \frac{n^2\pi^2}{6(3+\sqrt{3})}\left(\frac{t}{\ell}\right)^3 = 0.202\,\bar{\rho}^3, \tag{94}$$

where the end constraint factor $n = 0.682$ is detailed in Appendix A.4. Following the same procedure, it is possible to show that $(\sigma_{pl})_1 = (\sigma_{pl})_2$; however, the elastic buckling strength is different and given by:

$$\frac{(\sigma_{el})_1}{E_s} = \frac{n^2\pi^2}{9(3+\sqrt{3})}\left(\frac{t}{\ell}\right)^3 = 0.182\,\bar{\rho}^3, \tag{95}$$

where the end constraint factor is $n = 0.793$ for compression along x_1, please refer to Appendix A.4 for more details.

2.4.2. Shear

The deformation of the truncated-trihexagonal lattice in shear is characterised by three rotations and four displacements, see the unit cell in Fig. 7b. Here, the shear stress τ is replaced by an equivalent force:

$$F = \frac{(3+\sqrt{3})}{2}\tau b\ell. \tag{96}$$

The transverse force in bar *ef* is simply:

$$V_{ef} = \frac{12E_sI}{\ell^2}\left(\frac{\Delta_1}{\ell} - \theta_1\right) = F, \tag{97}$$

and that in bar *ac* and *bd* is given by:

$$V_{ac} = V_{bd} = \frac{6E_sI}{\ell^2}\left(\theta_3 - \theta_2 - \frac{2\Delta_4}{\ell}\right) = -\frac{F}{2}. \tag{98}$$

Also, the transverse forces in bars *aa* and *ee* have to respect:

$$V_{aa} + V_{ee} = \frac{12E_sI}{\ell^2}\left(\theta_3 - \theta_1 - \frac{2\Delta_2}{\ell}\right) = -\sqrt{3}F. \tag{99}$$

Moreover, equilibrium of moments at vertices a, b, and e return:

$$M_{aa} + M_{ab} + M_{ac} = \tfrac{2E_sI}{\ell}\left(7\theta_3 - 2\theta_2 + \tfrac{3}{\ell}(\Delta_3 - \Delta_2 - \Delta_4)\right) = 0, \tag{100}$$

$$M_{ba} + M_{bd} + M_{be} = \tfrac{2E_sI}{\ell}\left(2\theta_3 - 6\theta_2 - \theta_1 + \tfrac{3}{\ell}(2\Delta_3 - \Delta_4)\right) = 0, \tag{101}$$

$$M_{ef} + M_{ee} + M_{eb} = \tfrac{2E_sI}{\ell}\left(-8\theta_1 - \theta_2 + \tfrac{3}{\ell}(\Delta_1 + \Delta_3 - \Delta_2)\right) = 0, \tag{102}$$

respectively. Finally, compatibility of displacements in x_2 requires that:

$$\frac{\Delta_3}{2} - \frac{\sqrt{3}}{2}\Delta_4 - \Delta_2 = 0. \tag{103}$$

The displacement field is solved using the previous seven equations and this yields:

$$\theta_1 = \frac{9+59\sqrt{3}}{372(3+\sqrt{3})}\frac{F\ell^2}{E_sI}, \tag{104}$$

$$\theta_2 = \frac{107\sqrt{3}-45}{372(3+\sqrt{3})}\frac{F\ell^2}{E_sI}, \tag{105}$$

$$\theta_3 = \frac{36-19\sqrt{3}}{186(3+\sqrt{3})}\frac{F\ell^2}{E_sI}, \tag{106}$$

$$\Delta_1 = \frac{17+15\sqrt{3}}{62(3+\sqrt{3})}\frac{F\ell^3}{E_sI}, \tag{107}$$

$$\Delta_2 = \frac{39-\sqrt{3}}{186(3+\sqrt{3})}\frac{F\ell^3}{E_sI}, \tag{108}$$

$$\Delta_3 = \frac{101\sqrt{3}-15}{372(3+\sqrt{3})}\frac{F\ell^3}{E_sI}, \tag{109}$$

$$\Delta_4 = \frac{35-19\sqrt{3}}{124(3+\sqrt{3})}\frac{F\ell^3}{E_sI}. \tag{110}$$

With the above displacement field, we can compute the shear strain:

$$\gamma = \frac{2\Delta_1 - \Delta_4 + 3\sqrt{3}\Delta_3}{(3+3\sqrt{3})\ell} = \frac{8(21+4\sqrt{3})}{31(1+\sqrt{3})}\frac{\tau}{E_s}\left(\frac{\ell}{t}\right)^3, \tag{111}$$

and the shear modulus $G = \tau/\gamma$ becomes:

$$\frac{G}{E_s} = \frac{31(1+\sqrt{3})}{8(21+4\sqrt{3})}\left(\frac{t}{\ell}\right)^3 = 0.474\bar{\rho}^3. \tag{112}$$

The truncated-trihexagonal lattice is in-plane isotropic and we find that $G = E/(2(1+\nu))$.

The maximum bending moment in a truncated-trihexagonal lattice is:

$$M_{ee} = \frac{3(29+19\sqrt{3})}{186+62\sqrt{3}}F\ell, \tag{113}$$

and equating this to the fully plastic moment (Eq. (1)) returns the plastic collapse strength in shear, which is:

$$\frac{\tau_{pl}}{\sigma_{ys}} = \frac{31}{3(29+19\sqrt{3})}\left(\frac{t}{\ell}\right)^2 = 0.194\,\bar{\rho}^2. \tag{114}$$

2.5. Snub-square lattice

The snub-square lattice has three triangles and two squares meeting at each vertex, see Fig. 8, and therefore, it has a nodal connectivity $Z = 5$. Their and St-Pierre [32] have shown that its behaviour is stretching-dominated in compression, but it is bending-dominated in shear, as we will show below. This tessellation has a 4-fold rotational symmetry and consequently, its in-plane elastic properties are not isotropic [37]. Its relative density is given by:

$$\bar{\rho} = \frac{20}{(1+\sqrt{3})^2}\left(\frac{t}{\ell}\right) = 2.680\left(\frac{t}{\ell}\right). \tag{115}$$

2.5.1. Compression

The uniaxial compressive behaviour of the snub-square lattice was investigated previously by Their and St-Pierre [32]. Their analytical work revealed that the snub-square lattice is stretching-dominated in compression with an elastic modulus:

$$\frac{E_2}{E_s} = \frac{3}{4}\left(\frac{t}{\ell}\right) = 0.280\bar{\rho}. \tag{116}$$

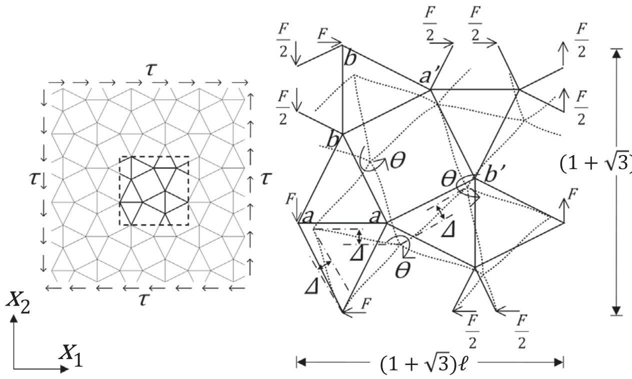

Fig. 8. Deformation of a snub-square lattice under shear.

Using the internal loads provided in Their and St-Pierre [32], we find that the Poisson's ratio is:

$$\nu_{12} = \frac{\sqrt{3}}{4} = 0.433. \tag{117}$$

In compression, the snub-square lattice can fail by either elastic buckling or yielding, depending on its relative density. The yield strength of the snub-square lattice is [32]:

$$\frac{(\sigma_{pl})_2}{\sigma_{ys}} = \frac{2}{(1+\sqrt{3})}\left(\frac{t}{\ell}\right) = 0.273\,\bar{\rho}, \tag{118}$$

whereas the elastic buckling strength is given by [32]:

$$\frac{(\sigma_{el})_2}{E_s} = \frac{n^2\pi^2}{6(1+\sqrt{3})}\left(\frac{t}{\ell}\right)^3 = 0.090\,\bar{\rho}^3, \tag{119}$$

where the end constraint factor $n = 1.693$ is derived analytically in Appendix A.5. Finally, note that $E_1 = E_2, (\sigma_{el})_1 = (\sigma_{el})_2$ and $(\sigma_{pl})_1 = (\sigma_{pl})_2$ due to symmetry.

2.5.2. Shear

In shear, the snub-square lattice deforms by bending, and the deformation of its unit cell is characterised by a deflection Δ and a rotation θ, see Fig. 8. The shear stress τ is replaced by an equivalent force:

$$F = \frac{(1+\sqrt{3})}{2}\tau b\ell. \tag{120}$$

Equilibrium of forces, along x_1, at vertex b requires that:

$$N_{ab} + \sqrt{3}V_{ab} = F, \tag{121}$$

$$\sqrt{3}N_{ba'} - V_{ba'} - V_{bb} = F, \tag{122}$$

where $N_{ab} = N_{ba'}$ is the axial load in bar ab. Combining these two equations to remove N_{ab} yields:

$$4V_{ba'} + V_{aa} = \frac{12E_sI}{\ell^2}\left(\frac{5\Delta}{\ell} - \theta\right) = (\sqrt{3}-1)F. \tag{123}$$

Otherwise, equilibrium of moments at vertex a gives:

$$2(M_{ab} + M_{ab'}) + M_{aa} = \frac{2E_sI}{\ell}\left(\frac{3\Delta}{\ell} - 7\theta\right) = 0. \tag{124}$$

Using the last two equations to find θ and Δ returns:

$$\theta = \frac{(\sqrt{3}-1)}{128}\frac{F\ell^2}{E_sI}, \tag{125}$$

$$\Delta = \frac{7(\sqrt{3}-1)}{384}\frac{F\ell^3}{E_sI}. \tag{126}$$

Next, the shear strain can be expressed as:

$$\gamma = \frac{2(\sqrt{3}-1)\Delta}{(\sqrt{3}+1)\ell} = \frac{7(\sqrt{3}-1)^2}{32}\frac{\tau}{E_s}\left(\frac{\ell}{t}\right)^3, \tag{127}$$

and the shear modulus becomes:

$$\frac{G_{12}}{E_s} = \frac{32}{7(\sqrt{3}-1)^2}\left(\frac{t}{\ell}\right)^3 = 0.443\bar{\rho}^3. \tag{128}$$

The maximum bending moment in a snub-square lattice subjected to shear is:

$$M_{ba} = \frac{\sqrt{3}-1}{8}F = \frac{1}{8}\tau b\ell, \tag{129}$$

and equating this to the fully plastic moment (Eq. (1)) returns the plastic collapse strength in shear:

$$\frac{\tau_{pl}}{\sigma_{ys}} = 2\left(\frac{t}{\ell}\right)^2 = 0.279\bar{\rho}^2. \tag{130}$$

2.6. Elongated-triangular lattice

The elongated-triangular lattice has three triangles and two squares meeting at each vertex, see Fig. 9; these are the same polygons as in a snub-square tessellation, but their arrangement is different. Therefore, the elongated-triangular lattice also has a nodal connectivity $Z = 5$, but it is clear, upon inspection, that its behaviour is stretching-dominated when compressed in x_1 or x_2, and bending-dominated in shear. Its elastic properties are not isotropic, and its relative density is:

$$\bar{\rho} = \frac{10}{(2+\sqrt{3})}\left(\frac{t}{\ell}\right) = 2.680\left(\frac{t}{\ell}\right), \tag{131}$$

which is the same as a snub-square lattice, see Eq. (115).

2.6.1. Compression

Consider the elongated-triangular lattice loaded in compression along the x_2 direction, see Fig. 9a. A unit cell is shown in Fig. 9a, where the nominal compressive stress σ is replaced by an equivalent force:

$$F = \sigma b\ell. \tag{132}$$

For this loading scenario, all bars are carrying axial forces only. Using the method of sections, it is straightforward to find the axial load in each bar and this gives:

$$N_{aa} = F, \tag{133a}$$

$$N_{ab} = N_{bc} = \frac{F}{\sqrt{3}}, \tag{133b}$$

$$N_{ac} = -\frac{F}{4\sqrt{3}}, \tag{133c}$$

where a negative sign indicates a tensile force. The shortening u of the unit cell is obtained by equating the work done by external forces to the internal energy. This gives:

$$u = \frac{1}{F}(N_{ab}\Delta_{ab} + N_{bc}\Delta_{bc} + N_{aa}\Delta_{aa} + 2N_{ac}\Delta_{ac}) = \frac{41}{24}\frac{F\ell}{E_sbt}, \tag{134}$$

where the shortening of bar ij is $\Delta_{ij} = N_{ij}\ell/(btE_s)$. Next, the nominal compressive strain in x_2 is:

$$\varepsilon_2 = \frac{u}{(1+\sqrt{3}/2)\ell} = \frac{41}{12(2+\sqrt{3})}\frac{\sigma}{E_s}\left(\frac{\ell}{t}\right), \tag{135}$$

and the elastic modulus $E_2 = \sigma/\varepsilon_2$ becomes:

$$\frac{E_2}{E_s} = \frac{12(2+\sqrt{3})}{41}\left(\frac{t}{\ell}\right) = 0.408\,\bar{\rho}. \tag{136}$$

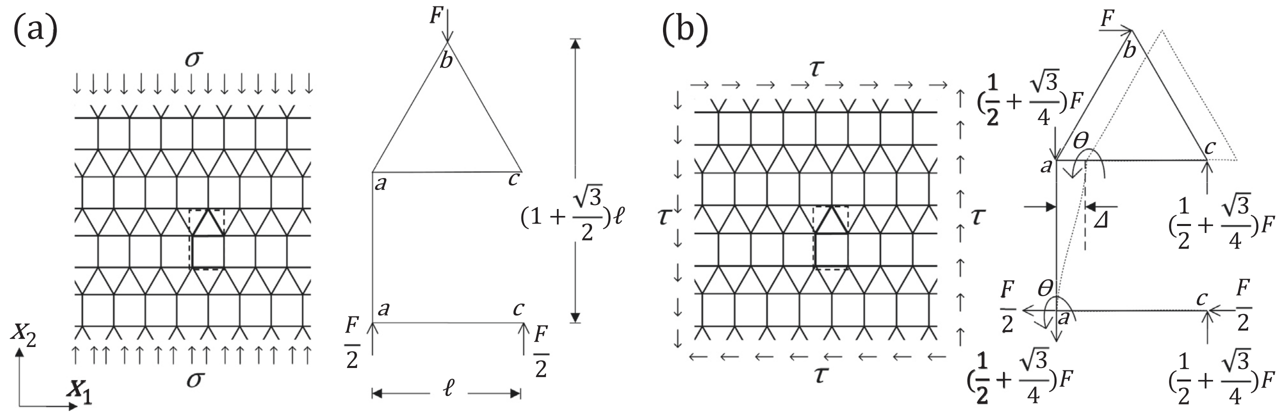

Fig. 9. Deformation of a elongated-triangle lattice under (a) compression and (b) shear.

Otherwise, the nominal strain in x_1 is:

$$\varepsilon_1 = \frac{\Delta_{ac}}{\ell} = -\frac{1}{4\sqrt{3}}\frac{\sigma}{E_s}\left(\frac{t}{\ell}\right), \tag{137}$$

which gives a Poisson's ratio:

$$\nu_{12} = -\frac{\varepsilon_1}{\varepsilon_2} = \frac{3+2\sqrt{3}}{41} = 0.158. \tag{138}$$

In compression, the elongated-triangular lattice fails by either elastic buckling or yielding depending on its relative density. For loading in x_2, the highest compressive force is in bar aa and setting $N_{aa} = \sigma_{ys}bt$ gives us the yield strength of the elongated-triangular lattice:

$$\frac{(\sigma_{pl})_2}{\sigma_{ys}} = \left(\frac{t}{\ell}\right) = 0.373\,\bar{\rho}. \tag{139}$$

Otherwise, equating N_{aa} to the Euler buckling load (Eq. (2)) returns the elastic buckling strength of the lattice:

$$\frac{(\sigma_{el})_2}{E_s} = \frac{n^2\pi^2}{12}\left(\frac{t}{\ell}\right)^3 = 0.033\bar{\rho}^3, \tag{140}$$

where the end constraint factor $n = 0.881$ is derived in Appendix A.6.

The same procedure can be followed to derive the properties for compression in x_1. In this case, the internal loads are:

$$N_{ac} = \frac{(2+\sqrt{3})}{4}\sigma b\ell, \tag{141a}$$

$$N_{aa} = N_{ab} = N_{bc} = 0, \tag{141b}$$

and the elastic modulus becomes:

$$\frac{E_1}{E_s} = \frac{4}{2+\sqrt{3}}\left(\frac{t}{\ell}\right) = 0.400\bar{\rho}, \tag{142}$$

which is almost equal to E_2. Otherwise, the yield strength is:

$$\frac{(\sigma_{pl})_1}{\sigma_{ys}} = \frac{4}{2+\sqrt{3}}\left(\frac{t}{\ell}\right) = 0.400\,\bar{\rho}, \tag{143}$$

whereas the elastic buckling strength is given by:

$$\frac{(\sigma_{el})_1}{E_s} = \frac{n^2\pi^2}{3(2+\sqrt{3})}\left(\frac{t}{\ell}\right)^3 = 0.105\,\bar{\rho}^3, \tag{144}$$

where the end constraint factor $n = 1.515$ is derived in Appendix A.6.

2.6.2. Shear

In shear, the elongated-triangular lattice deforms by bending bar aa, see Fig. 9b. The deformation of the unit cell is characterised by only two variables: the transverse deflection Δ and rotation θ of beam aa. The shear stress τ can be replaced by an equivalent force:

$$F = \tau b\ell, \tag{145}$$

and the transverse load in beam aa can be expressed as:

$$V_{aa} = \frac{12E_sI}{\ell^2}\left(\frac{\Delta}{\ell} - \theta\right) = F. \tag{146}$$

Moreover, equilibrium of moments at vertex a gives:

$$2(M_{ab} + M_{ac}) + M_{aa} = \frac{6E_sI}{\ell}\left(\frac{\Delta}{\ell} - 5\theta\right) = 0. \tag{147}$$

Using the last two equations to solve for θ and Δ returns:

$$\theta = \frac{F\ell^2}{48E_sI}, \tag{148}$$

$$\Delta = \frac{5F\ell^3}{48E_sI}. \tag{149}$$

Next, the shear strain is given by:

$$\gamma = \frac{\Delta}{(1+\sqrt{3}/2)\ell} = \frac{5}{2(2+\sqrt{3})}\frac{\tau}{E_s}\left(\frac{\ell}{t}\right)^3, \tag{150}$$

and the shear modulus becomes:

$$\frac{G_{12}}{E_s} = \frac{2(2+\sqrt{3})}{5}\left(\frac{t}{\ell}\right)^3 = 0.078\bar{\rho}^3. \tag{151}$$

In shear, the maximum bending moment in an elongated-triangular lattice is:

$$M_{aa} = \frac{F\ell}{2} = \frac{\tau b\ell^2}{2}, \tag{152}$$

and equating this to the fully plastic moment (Eq. (1)) gives us the plastic collapse strength of the lattice in shear:

$$\frac{\tau_{pl}}{\sigma_{ys}} = \frac{1}{2}\left(\frac{t}{\ell}\right)^2 = 0.070\,\bar{\rho}^2. \tag{153}$$

2.7. Snub-trihexagonal lattice

A snub-trihexagonal lattice has four triangles and a hexagon meeting at each vertex, see Fig. 10. It has a nodal connectivity $Z = 5$, and our analysis below will show that its behaviour is stretching-dominated in both compression and shear. Its elastic

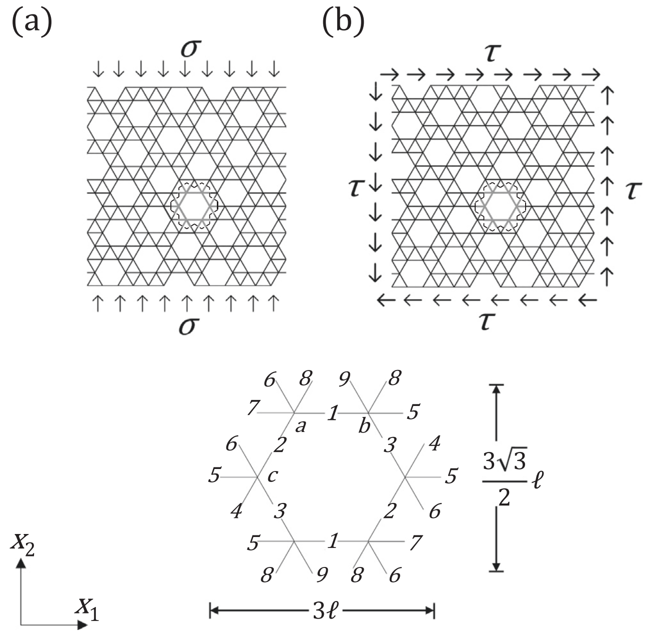

Fig. 10. A snub-trihexagonal lattice under (a) compression and (b) shear.

properties are isotropic since this pattern has a 6-fold rotational symmetry [37]. Its relative density is given by:

$$\bar{\rho} = \frac{10\sqrt{3}}{7}\left(\frac{t}{\ell}\right) = 2.474\left(\frac{t}{\ell}\right). \tag{154}$$

2.7.1. Compression

In compression, the cell walls of the snub-trihexagonal lattice are carrying axial forces only. The unit cell, shown in Fig. 10a, includes nine independent bars and their axial loads are labelled $N_1, N_2, \ldots, N_9$. Equilibrium equations at vertices a, b and c give:

$$2N_1 - N_2 - N_6 - 2N_7 + N_8 = 0, \tag{155a}$$

$$-N_2 + N_6 + N_8 = 0, \tag{155b}$$

$$-2N_1 + N_3 + 2N_5 + N_8 - N_9 = 0, \tag{155c}$$

$$-N_3 + N_8 + N_9 = 0, \tag{155d}$$

$$-N_2 - N_3 + N_4 + 2N_5 + N_6 = 0, \tag{155e}$$

$$-N_2 + N_3 + N_4 - N_6 = 0. \tag{155f}$$

Next, the macroscopic stress field is $\sigma_{11} = 0, \sigma_{12} = 0$, and $\sigma_{22} = \sigma$, and these give:

$$4N_1 + N_2 + N_3 + \tfrac{N_4}{2} + 4N_5 + N_6 + 2N_7 + N_8 + \tfrac{N_9}{2} = 0, \tag{156}$$

$$2N_2 - 2N_3 + N_4 - 2N_6 + 2N_8 - N_9 = 0, \tag{157}$$

$$2N_2 + 2N_3 + N_4 + 2N_6 + 2N_8 + N_9 = \tfrac{14}{\sqrt{3}}\sigma b\ell, \tag{158}$$

respectively. The previous nine equations are used to solve for the axial forces, and this returns:

$$N_1 = -\frac{\sqrt{3}}{12}\sigma b\ell, N_2 = \frac{2\sqrt{3}}{3}\sigma b\ell, \tag{159a}$$

$$N_3 = \frac{5\sqrt{3}}{12}\sigma b\ell, N_4 = \frac{5\sqrt{3}}{6}\sigma b\ell, \tag{159b}$$

$$N_5 = -\frac{\sqrt{3}}{6}\sigma b\ell, N_6 = \frac{7\sqrt{3}}{12}\sigma b\ell, \tag{159c}$$

$$N_7 = -\frac{2\sqrt{3}}{3}\sigma b\ell, N_8 = \frac{\sqrt{3}}{12}\sigma b\ell, \tag{159d}$$

$$N_9 = \frac{\sqrt{3}}{3}\sigma b\ell, \tag{159e}$$

where a negative sign indicates tension. Next, the nominal compressive strain can be obtained by equating the work done by the external load to the internal strain energy, and this gives:

$$\begin{aligned}\varepsilon_2 &= \tfrac{2}{7\sqrt{3}}\tfrac{1}{E_s\sigma b^2 t\ell}\Big(2N_1^2 + 2N_2^2 + 2N_3^2 + \\ &N_4^2 + 2N_5^2 + 2N_6^2 + N_7^2 + 2N_8^2 + N_9^2\Big) = \tfrac{13\sqrt{3}}{14}\tfrac{\sigma}{E_s}\left(\tfrac{\ell}{t}\right).\end{aligned} \tag{160}$$

Finally, the elastic modulus becomes:

$$\frac{E}{E_s} = \frac{14\sqrt{3}}{39}\left(\frac{t}{\ell}\right) = 0.251\,\bar{\rho}. \tag{161}$$

Using the principle of virtual work, we find that the strain along x_1 is:

$$\begin{aligned}\varepsilon_1 &= \frac{1}{7\ell}(3\Delta_1 + \Delta_3 - \Delta_4 + 2\Delta_5 - \Delta_6 + 2\Delta_7 + \Delta_8) \\ &= -\frac{17\sqrt{3}}{42}\frac{\sigma}{E_s}\left(\frac{\ell}{t}\right),\end{aligned} \tag{162}$$

where $\Delta_i = N_i\ell/(btE_s)$ is the extension/shortening of bar i. With this result, the Poisson's ratio becomes:

$$\nu = -\frac{\varepsilon_1}{\varepsilon_2} = \frac{17}{39} = 0.436. \tag{163}$$

The snub-trihexagonal lattice fails by elastic buckling or yielding depending on the relative density. For compression in x_2, bar 4 carries the highest compressive force. Setting $N_4 = \sigma_{ys}bt$ gives us the yield strength of the lattice:

$$\frac{(\sigma_{pl})_2}{\sigma_{ys}} = \frac{2\sqrt{3}}{5}\left(\frac{t}{\ell}\right) = 0.280\,\bar{\rho}. \tag{164}$$

Otherwise, equating N_4 to the Euler buckling load (Eq. (2)) returns the elastic buckling strength:

$$\frac{(\sigma_{el})_2}{E_s} = \frac{n^2\pi^2}{10\sqrt{3}}\left(\frac{t}{\ell}\right)^3 = 0.089\,\bar{\rho}^3, \tag{165}$$

where the end constraint factor $n = 1.541$ is derived analytically in Appendix A.7.

The same procedure can be used for uniaxial compression in x_1. For this loading scenario, the internal loads are:

$$N_1 = \frac{3\sqrt{3}}{4}\sigma b\ell, N_2 = 0, \tag{166a}$$

$$N_3 = \frac{\sqrt{3}}{4}\sigma b\ell, N_4 = -\frac{\sqrt{3}}{2}\sigma b\ell, \tag{166b}$$

$$N_5 = \frac{\sqrt{3}}{2}\sigma b\ell, N_6 = -\frac{\sqrt{3}}{4}\sigma b\ell, \tag{166c}$$

$$N_7 = \sqrt{3}\sigma b\ell, N_8 = \frac{\sqrt{3}}{4}\sigma b\ell, \tag{166d}$$

$$N_9 = 0. \tag{166e}$$

Of course, we find the same elastic modulus in x_1 since this topology is isotropic. Here, the highest compressive load is in bar 7, and setting $N_7 = \sigma_{ys}bt$ returns the yield strength:

$$\frac{(\sigma_{pl})_1}{\sigma_{ys}} = \frac{1}{\sqrt{3}}\left(\frac{t}{\ell}\right) = 0.233\,\bar{\rho}. \tag{167}$$

Finally, equating N_7 to the Euler buckling load (Eq. (2)) yields the elastic buckling strength:

$$\frac{(\sigma_{el})_1}{E_s} = \frac{n^2\pi^2}{12\sqrt{3}}\left(\frac{t}{\ell}\right)^3 = 0.087\,\bar{\rho}^3, \tag{168}$$

where the end constraint factor $n = 1.661$ is derived in Appendix A.7.

2.7.2. Shear

In shear, the cell walls of the snub-trihexagonal lattice also carry axial forces only. The unit cell includes nine independent bars and these are identified in Fig. 10b. The six equilibrium equations in (155) are also valid for shear. Otherwise, the macroscopic stress field is $\sigma_{12} = \tau, \sigma_{22} = 0$, and $\sigma_{11} = 0$, and these give:

$$-N_2 + N_3 - \frac{N_4}{2} + N_6 - N_8 + \frac{N_9}{2} = 7\tau b\ell, \tag{169}$$

$$2N_2 + 2N_3 + N_4 + 2N_6 + 2N_8 + N_9 = 0, \tag{170}$$

$$4N_1 + N_2 + N_3 + \tfrac{N_4}{2} + 4N_5 + N_6 + 2N_7 + N_8 + \tfrac{N_9}{2} = 0, \tag{171}$$

respectively. With these three equations and those in (155), we can solve for the nine axial forces, which returns:

$$N_1 = -\frac{1}{2}\tau b\ell, N_2 = -\tau b\ell, \tag{172a}$$

$$N_3 = \frac{3}{2}\tau b\ell, N_4 = -2\tau b\ell, \tag{172b}$$

$$N_5 = \tau b\ell, N_6 = \frac{1}{2}\tau b\ell, \tag{172c}$$

$$N_7 = -\tau b\ell, N_8 = -\frac{3}{2}\tau b\ell, \tag{172d}$$

$$N_9 = 3\tau b\ell, \tag{172e}$$

where a negative sign denotes tension. Then, the shear strain is obtained by equating the work done by external forces to the strain energy, and this yields:

$$\begin{aligned} \gamma \quad &= \tfrac{2}{7\sqrt{3}\ell b^2 t E_s \tau}\Big(2N_1^2 + 2N_2^2 + 2N_3^2 + N_4^2 + 2N_5^2 \\ &\quad + 2N_6^2 + N_7^2 + 2N_8^2 + N_9^2\Big) = \tfrac{8}{\sqrt{3}}\tfrac{\tau}{E_s}\left(\tfrac{\ell}{t}\right). \end{aligned} \tag{173}$$

Finally, the shear modulus becomes:

$$\frac{G}{E_s} = \frac{\sqrt{3}}{8}\left(\frac{t}{\ell}\right) = 0.088\,\bar{\rho}. \tag{174}$$

The relationship $G = E/(2(1 + v))$ is respected since the snub-trihexagonal lattice is in-plane isotropic.

In shear, bar 9 carries the highest (compressive) load. Setting $N_9 = \sigma_{ys} bt$ gives us the yield strength of the lattice:

$$\frac{\tau_{pl}}{\sigma_{ys}} = \frac{1}{3}\left(\frac{t}{\ell}\right) = 0.135\,\bar{\rho}, \tag{175}$$

whereas equating N_9 to the Euler buckling load (Eq. (2)) returns the elastic buckling strength:

$$\frac{\tau_{el}}{E_s} = \frac{n^2\pi^2}{36}\left(\frac{t}{\ell}\right)^3 = 0.055\,\bar{\rho}^3, \tag{176}$$

where the end constraint factor $n = 1.741$ is derived analytically in Appendix A.7.

3. Finite Element modelling

Finite Element simulations were conducted to validate the analytical expressions derived in Section 2. All simulations were done using the implicit solver of the commercial software Abaqus 6.18. The parent material was modelled as an isotropic linear elastic, perfectly-plastic solid with a Young's modulus $E_s = 200$ GPa, a Poisson's ratio $v = 0.3$ and a yield strength $\sigma_{ys} = 200$ MPa. For each topology, the relative density was varied from 0.01 to 0.3 by changing the thickness t of the cell walls, while keeping their length fixed at $\ell = 10$ mm. The cell walls were discretised using shear-flexible Timoshenko beam elements (B21 in Abaqus notation), and a mesh convergence study showed that ten elements per bar (corresponding to a mesh size of 1 mm) offers accurate predictions, see Supplementary material. All simulations included a small geometric imperfection, which had the shape of the first eigenmode and an amplitude of 0.05t. This small imperfection was necessary to trigger buckling, but had a negligible effect on the stiffness of the lattice.

Each topology was modelled using a periodic unit cell (see Fig. S1 in Supplementary material). Periodicity was enforced with the following equations [26]:

$$\Delta u_i = \epsilon_{ij}\Delta x_j \quad \text{and} \quad \Delta\theta = 0, \tag{177}$$

where Δu_i and $\Delta\theta$ are the differences in displacement and rotation, respectively, between two corresponding points on either sides of the unit cell; Δx_j is the vector connecting these two corresponding points; and ϵ_{ij} is the macroscopic strain tensor. The compressive response along x_2 was simulated by prescribing ϵ_{22} and letting Abaqus calculate σ_{22} provided that $\sigma_{11} = \sigma_{12} = 0$. Similarly, the compressive response in x_1 was obtained by setting ϵ_{11} and calculating σ_{11} with $\sigma_{22} = 0$. Otherwise, the response in shear was obtained by imposing ϵ_{12} and computing σ_{12} while ensuring that $\sigma_{11} = \sigma_{22} = 0$. More details on how these periodic boundary conditions were implemented in Abaqus are given in Supplementary material.

4. Results and discussion

4.1. Comparison between analytical and Finite Element results

Analytical results are compared to FE simulations in Fig. 11, where four properties (E_2; σ_2; G_{12}; and τ_{12}) are plotted as a function of relative density. In each plot, results are shown for all eight semi-regular lattices (including, for completeness, the trihexagonal tessellation even though its properties were derived analytically by Wang and McDowell [25], Fan et al. [23]). For each topology, there is an excellent agreement between analytical and FE predictions, and this holds true for the four properties plotted in Fig. 11. Note that there is also an excellent agreement between analytical and FE results for E_1 and σ_1, but these results are not shown here for the sake of brevity and because $E_1 = E_2$ and $\sigma_1 = \sigma_2$ for many topologies.

Our analytical work predicts that the failure mode of stretching-dominated lattices will switch from yielding to elastic buckling as the relative density decreases. This transition is clearly visible in Fig. 11b,d and for both failure modes, there is an excellent agreement between analytical and FE predictions. Based on our analytical modelling, the compressive strength σ_2 of bending-dominated lattices should display a similar transition (from plastic collapse to elastic buckling) but this switch is not visible in Fig. 11b because it occurs at $\bar{\rho} < 0.01$ for this choice of material properties where $\sigma_{ys}/E_s = 0.001$. The relative density at which the failure mode changes to elastic buckling is sensitive to σ_{ys}/E_s [21]; therefore additional FE simulations were performed with $\sigma_{ys}/E_s = 0.01$ to capture this transition for bending-dominated lattices. These results are provided in Appendix B and show a very good agreement between analytical and FE predictions.

Note that the FE simulations presented here are done using Timoshenko beam elements, which account for axial, bending and shear deformations. In contrast, our analytical model neglects

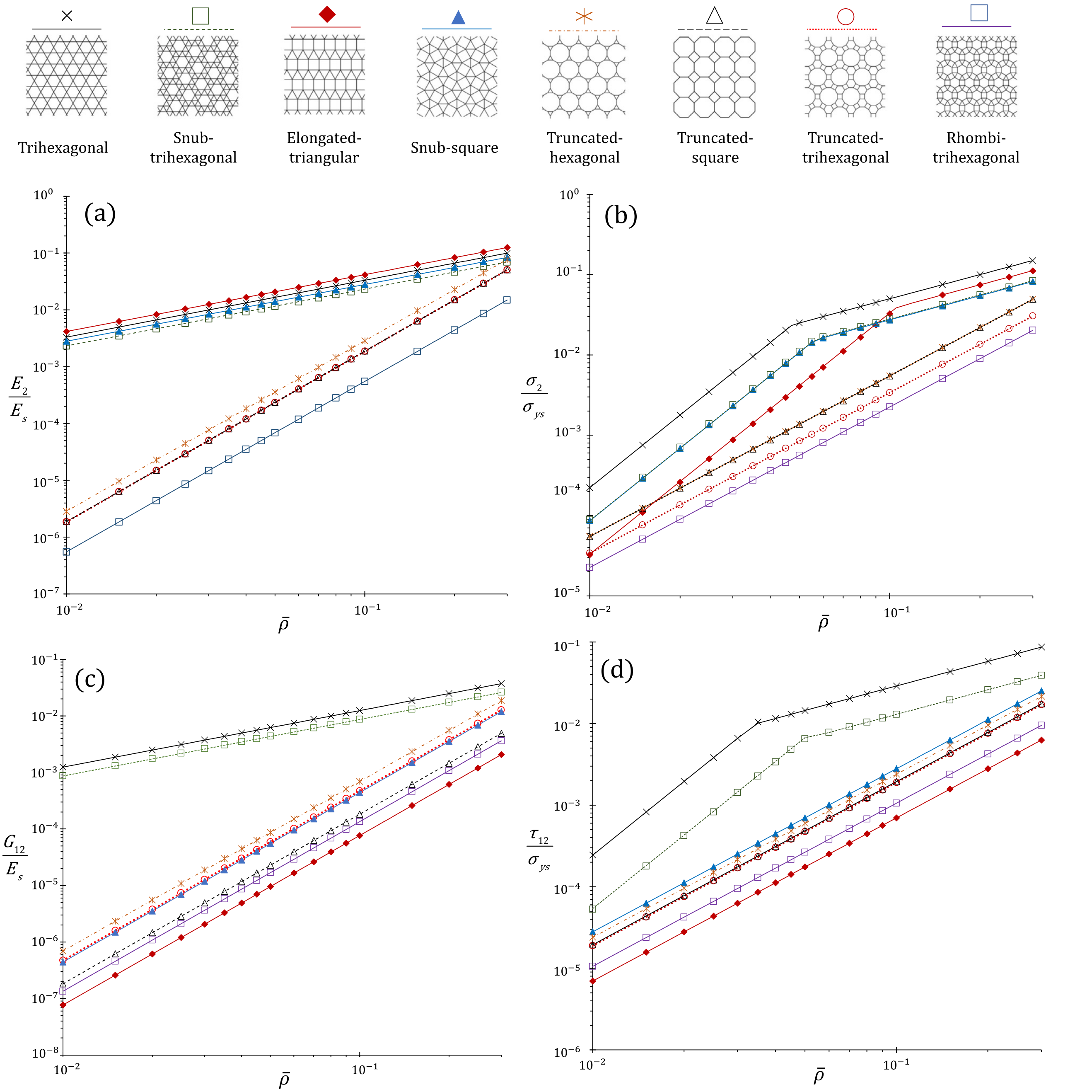

Fig. 11. Comparison between analytical (lines) and FE (symbols) results for the normalised mechanical properties of semi-regular lattices: (a) elastic modulus E_2, (b) compressive strength σ_2, (c) shear modulus G_{12}, and (d) shear strength τ_{12}, all plotted as a function of relative density $\bar{\rho}$. The properties of the parent material are $E_s = 200\,\text{GPa}$ and $\sigma_{ys} = 200\,\text{MPa}$.

(i) axial and shear deformations inside the cell walls of bending-dominated lattices and (ii) bending and shear deformations for the bars of stretching-dominated topologies (see Section 2). These assumptions are justified based on the excellent agreement between analytical and FE results, see Fig. 11 and Appendix B. Therefore, we conclude that the analytical expressions derived in Section 2 are validated for relative densities ranging from 0.01 to 0.3.

4.2. Comparison between regular and semi-regular lattices

The mechanical properties of all eight semi-regular lattices are compared to those of regular tessellations in Table 1. Topologies are divided in three groups depending on their behaviour: (i) bending-dominated lattices; (ii) topologies that are stretching-dominated in compression, but bending-dominated in shear; and (iii) stretching-dominated lattices. Below, we discuss each group in turn.

Four of the eight semi-regular lattices have a bending-dominated behaviour, and their properties are compared to those of a regular hexagonal tessellation in Table 1. Note that all bending-dominated lattices are in-plane elastically isotropic, except for the truncated-square topology. Amongst all bending-dominated lattices, the truncated-hexagonal tessellation clearly offers the best performances: it is 85% stiffer than a hexagonal lattice and has a slightly higher plastic collapse strength. This is true

Table 1
The mechanical properties of all eight semi-regular lattices are compared to those of regular tessellations (hexagonal, square and triangular). A reference frame is included in Fig. 1 for regular lattices. Expressions for regular topologies and for the trihexagonal lattice are taken from Gibson and Ashby [21], Wang and McDowell [23], Fan et al. [25].

Topology	$\frac{\bar{\rho}}{t/\ell}$	$\frac{E_2}{E_s}$	ν_{12}	$\frac{G_{12}}{E_s}$	$\frac{(\sigma_{pl})_2}{\sigma_{ys}}$	$\frac{(\sigma_{pl})_1}{\sigma_{ys}}$	$\frac{(\sigma_{el})_2}{E_s}$	$\frac{(\sigma_{el})_1}{E_s}$	$\frac{(\tau_{pl})}{\sigma_{ys}}$	$\frac{(\tau_{el})}{E_s}$
Bending-dominated topologies										
Hexagonal	1.154	$1.500\bar{\rho}^3$	1	$0.375\bar{\rho}^3$	$0.500\bar{\rho}^2$	$0.500\bar{\rho}^2$	$0.145\bar{\rho}^3$	-	$0.217\bar{\rho}^2$	-
Truncated-hexagonal	0.746	$2.780\bar{\rho}^3$	1	$0.695\bar{\rho}^3$	$0.556\bar{\rho}^2$	$0.556\bar{\rho}^2$	$0.082\bar{\rho}^3$	-	$0.243\bar{\rho}^2$	-
Rhombi-trihexagonal	1.856	$0.542\bar{\rho}^3$	1	$0.135\bar{\rho}^3$	$0.221\bar{\rho}^2$	$0.221\bar{\rho}^2$	$0.071\bar{\rho}^3$	-	$0.106\bar{\rho}^2$	-
Truncated-square	1.029	$1.833\bar{\rho}^3$	1	$0.183\bar{\rho}^3$	$0.553\bar{\rho}^2$	$0.553\bar{\rho}^2$	$0.168\bar{\rho}^3$	$0.168\bar{\rho}^3$	$0.195\bar{\rho}^2$	-
Truncated-trihexagonal	0.928	$1.896\bar{\rho}^3$	1	$0.474\bar{\rho}^3$	$0.411\bar{\rho}^2$	$0.411\bar{\rho}^2$	$0.202\bar{\rho}^3$	$0.182\bar{\rho}^3$	$0.194\bar{\rho}^2$	-
Stretching-dominated in compression and bending-dominated in shear										
Square	2.000	$0.500\bar{\rho}$	$0.5\nu_s\bar{\rho}$	$0.063\bar{\rho}^3$	$0.500\bar{\rho}$	$0.500\bar{\rho}$	$0.059\bar{\rho}^3$	$0.059\bar{\rho}^3$	$0.125\bar{\rho}^2$	-
Snub-square	2.680	$0.280\bar{\rho}$	0.433	$0.443\bar{\rho}^3$	$0.273\bar{\rho}$	$0.273\bar{\rho}$	$0.090\bar{\rho}^3$	$0.090\bar{\rho}^3$	$0.279\bar{\rho}^2$	-
Elongated-triangular	2.680	$0.408\bar{\rho}$	0.158	$0.078\bar{\rho}^3$	$0.373\bar{\rho}$	$0.400\bar{\rho}$	$0.033\bar{\rho}^3$	$0.105\bar{\rho}^3$	$0.070\bar{\rho}^2$	-
Stretching-dominated topologies										
Triangular	3.464	$0.333\bar{\rho}$	0.333	$0.125\bar{\rho}$	$0.500\bar{\rho}$	$0.333\bar{\rho}$	$0.069\bar{\rho}^3$	$0.061\bar{\rho}^3$	$0.289\bar{\rho}$	$0.051\bar{\rho}^3$
Trihexagonal (Kagome)	1.732	$0.333\bar{\rho}$	0.333	$0.125\bar{\rho}$	$0.500\bar{\rho}$	$0.333\bar{\rho}$	$0.224\bar{\rho}^3$	$0.194\bar{\rho}^3$	$0.289\bar{\rho}$	$0.244\bar{\rho}^3$
Snub-trihexagonal	2.474	$0.251\bar{\rho}$	0.436	$0.088\bar{\rho}$	$0.280\bar{\rho}$	$0.233\bar{\rho}$	$0.089\bar{\rho}^3$	$0.087\bar{\rho}^3$	$0.135\bar{\rho}$	$0.055\bar{\rho}^3$

for both compression and shear. The truncated-hexagonal has a lower elastic buckling strength than a hexagonal lattice, but this failure mode occurs only at low values of relative densities. Otherwise, the truncated-square and truncated-trihexagonal lattices have performances that are similar to those of the hexagonal topology. Finally, the rhombi-trihexagonal tessellation has by far the lowest properties: it is three times more compliant and about two times weaker than the hexagonal lattice.

Two semi-regular topologies, the elongated-triangular and the snub-square lattices, are stretching-dominated in compression along x_1 or x_2, but bending-dominated in shear. The elongated-triangular topology has similar properties to a regular square lattice: they both have a high elastic modulus and compressive strength in x_1 or x_2, but they are very compliant in shear. In contrast, the snub-square lattice has a shear modulus about five times higher than that of the elongated-triangular and square topologies, but its elastic modulus and compressive strength are lower.

Finally, only two semi-regular tessellations have a stretching-dominated behaviour: trihexagonal and snub-trihexagonal lattices. Their properties are compared to those of a regular triangular lattice in Table 1. Note that these three lattices are in-plane elastically isotropic. The snub-trihexagonal lattice is 30% more compliant and has a lower yield strength than the triangular and trihexagonal topologies (which have identical values for $E_2; G_{12}; (\sigma_{pl})_1$ and $(\sigma_{pl})_2$). The three lattices differ in their resistance to elastic buckling: the snub-trihexagonal lattice is 43% stronger than a triangular lattice, but weaker than a trihexagonal topology.

5. Conclusion

The in-plane mechanical properties of seven semi-regular lattices were presented in this study. For each topology, analytical expressions were derived for the elastic modulus and strength under uniaxial compression and shear. These analytical equations were then verified with finite element simulations.

The analysis allowed us to classify the behaviour of these seven tessellations: four were found to be bending-dominated; one was stretching-dominated; and two were stretching-dominated in compression but bending-dominated in shear. The properties of these seven semi-regular tessellations were also compared to those of regular lattices, and this revealed the potential of the truncated-hexagonal lattice. The truncated-hexagonal tessellation is elastically isotropic and it is 85% stiffer and 11% stronger than its hexagonal counterpart. With such combination of properties, the truncated-hexagonal lattice is a promising topology for automotive, rail and aerospace applications where a high stiffness and strength are required. Finally, work is underway to manufacture these semi-regular lattices and measure the properties derived in this study.

6. Data availability

The raw/processed data required to reproduce these findings cannot be shared at this time as the data also forms part of an ongoing study.

Declaration of Competing Interest

The authors declare that they have no known competing financial interests or personal relationships that could have appeared to influence the work reported in this paper.

Acknowledgements

The authors are grateful for the financial support from the Academy of Finland (decision 322007).

Appendix A. End constraint factor

At low relative densities, lattices often fail by elastic buckling. This occurs when the compressive force in a bar reaches the Euler buckling load, Eq. (2), which is a function of the end constraint factor n. The end constraint factor n was derived analytically by Fan et al. [25] for square, triangular, and trihexagonal lattices, and here, we extend their analysis to other semi-regular topologies.

The approach used by Fan et al. [25] to derive n is based on an extension of the stiffness matrix introduced earlier in Eq. (3). Consider that an axial compressive load P is added to the beam shown in Fig. 3. This force affects the stiffness matrix, which becomes [36]:

$$\begin{Bmatrix} M_{ij} \\ M_{ji} \\ V_{ij} \end{Bmatrix} = \frac{E_s I}{\ell} \begin{bmatrix} s & sc & \bar{s}/\ell \\ sc & s & \bar{s}/\ell \\ \bar{s}/\ell & \bar{s}/\ell & s^*/\ell^2 \end{bmatrix} \begin{Bmatrix} \theta_i \\ \theta_j \\ \Delta_{ij} \end{Bmatrix}, \tag{178}$$

where s^*, and $\bar{s}$ are:

$$s^* = 2\bar{s} - \frac{P\ell^2}{E_s I}, \tag{179}$$

and

$$\bar{s} = s(1 + c), \tag{180}$$

respectively, and where the parameters s and c depend on the axial load P. In compression $(P > 0)$, s and c are given by:

$$s = \frac{\lambda(\sin\lambda - \lambda\cos\lambda)}{2 - 2\cos\lambda - \lambda\sin\lambda}, \tag{181}$$

$$c = \frac{\lambda - \sin\lambda}{\sin\lambda - \lambda\cos\lambda}, \tag{182}$$

where λ is related to the load P and the end constraint factor n via:

$$\lambda = \sqrt{\frac{P\ell^2}{E_s I}} = n\pi. \tag{183}$$

Otherwise, for tension $(P < 0)$, the coefficients become:

$$s = s_1 = \frac{\lambda_1(\lambda_1\cosh\lambda_1 - \sinh\lambda_1)}{2 - 2\cosh\lambda_1 + \lambda_1\sinh\lambda_1}, \tag{184}$$

$$c = c_1 = \frac{\sinh\lambda_1 - \lambda_1}{\lambda\cosh\lambda_1 - \sinh\lambda_1}, \tag{185}$$

where:

$$\lambda_1 = \sqrt{\frac{-P\ell^2}{E_s I}}. \tag{186}$$

Note that the subscript 1 is used only to differentiate between tension and compression. Finally, if $P = 0$, we have:

$$s = 4, \; c = 0.5, \tag{187}$$

and the stiffness matrix returns to Eq. (3).

The procedure to derive the end constraint factor n is as follows. For a given topology and loading direction, the periodic buckling mode with the longest wavelength is identified[1]. Then, equilibrium conditions are combined with Eq. (178) to obtain a constitutive equation where λ is the only unknown. Solving for λ, it is then straightforward to compute the end buckling constraint since $n = \lambda/\pi$, see Eq. (183).

A.1. Truncated-hexagonal lattice

When compressed in x_2, the truncated-hexagonal lattice is anticipated to buckle in the swaying mode shown Fig. 12. Equilibrium of moments at vertices a and b, and the transverse forces in bars aa and ab give the following set of equations:

$$\begin{cases} M_{aa} + 2M_{ab} = 0, \\ M_{ba} + M_{bb} + M_{bc} = 0, \\ V_{aa} = 0, \\ V_{ab} - \frac{E_s I}{4}\left(\frac{\lambda_{aa}}{\ell}\right)^2 = 0, \end{cases} \tag{188}$$

[1] While the analysis in this appendix is entirely analytical, we have verified, using FE eigenvalue buckling predictions, that the anticipated buckling patterns corresponds to the first eigenmode for each topology.

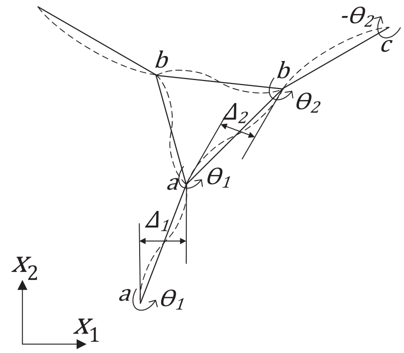

Fig. 12. Buckling mode of a truncated-hexagonal lattice compressed in x_2.

where each moment and transverse force can be expressed as a function of $\theta_1, \theta_2, \Delta_1$ and Δ_2 using Eq. (178). This gives:

$$M_{aa} = \frac{E_s I}{\ell}\left(s_{aa}(1 + c_{aa})\,\theta_1 + \frac{\bar{s}_{aa}}{\ell}\,\Delta_1\right), \tag{189a}$$

$$M_{ab} = \frac{E_s I}{\ell}\left(s_{ab}\,\theta_1 + s_{ab}c_{ab}\,\theta_2 + \frac{\bar{s}_{ab}}{\ell}\,\Delta_2\right), \tag{189b}$$

$$M_{ba} = \frac{E_s I}{\ell}\left(s_{ab}c_{ab}\,\theta_1 + s_{ab}\,\theta_2 + \frac{\bar{s}_{ab}}{\ell}\,\Delta_2\right), \tag{189c}$$

$$M_{bb} = \frac{E_s I}{\ell}\,s_{1bb}(1 + c_{1bb})\,\theta_2, \tag{189d}$$

$$M_{bc} = \frac{E_s I}{\ell}\,s_{bc}(1 - c_{bc})\,\theta_2, \tag{189e}$$

$$V_{aa} = \frac{E_s I}{\ell}\left(2\frac{\bar{s}_{aa}}{\ell}\,\theta_1 + \frac{s^*_{aa}}{\ell^2}\Delta_1\right), \tag{189f}$$

$$V_{ab} = \frac{E_s I}{\ell}\left(\frac{\bar{s}_{ab}}{\ell}\,(\theta_1 + \theta_2) + \frac{s^*_{ab}}{\ell^2}\Delta_2\right), \tag{189g}$$

where $\bar{s}_{ij}, s^*_{ij}, s_{ij}$ and c_{ij} are all functions of λ_{ij} as defined in Eqs. (179)–(186). Substituting Eq. (189) in (188) returns a linear system of equations: $\boldsymbol{A}[\theta_1, \theta_2, \Delta_1, \Delta_2]^T = \mathbf{0}$, where the determinant of $\boldsymbol{A}$ should be zero for a non-trivial solution to exists. Setting $\det(\boldsymbol{A}) = 0$ returns a lengthy expression that includes $\lambda_{aa}, \lambda_{ab}, \lambda_{bb}$, and λ_{bc}. Each λ_{ij} is proportional to the axial load in bar ij (see Eq. (183)); therefore, using structural analysis, we find that:

$$\begin{cases} \lambda_{ab}^2 = 0.702\,\lambda_{aa}^2, \\ \lambda_{1bb}^2 = 0.538\,\lambda_{aa}^2, \\ \lambda_{bc}^2 = 0.250\,\lambda_{aa}^2. \end{cases} \tag{190}$$

Above, each λ_{ij} is expressed as a function of λ_{aa}, since bar aa is the most loaded strut and the one expected to buckle. Substituting Eq. (190) in $\det(\boldsymbol{A}) = 0$ yields an expression where λ_{aa} is the only unknown. Solving this numerically gives $\lambda_{aa} = 1.240$, and consequently, the end constrain factor for a truncated-hexagonal lattice compressed in x_2 is:

$$n = \frac{\lambda_{aa}}{\pi} = 0.394. \tag{191}$$

A.2. Rhombi-trihexagonal lattice

A rhombi-trihexagonal lattice is expected to buckle elastically in the swaying mode shown Fig. 13 when compressed in x_2. The buckling shape is characterised by rotations θ_1 and θ_2, and a lateral displacement Δ. Equilibrium of moments at vertices a and b, as well as the transverse load in bar ae return the following set of equations:

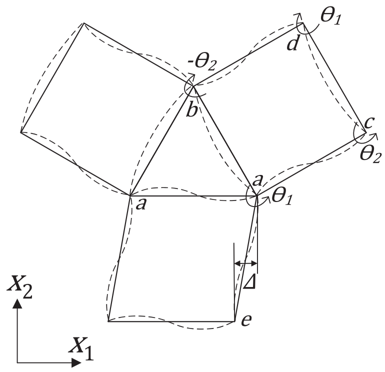

Fig. 13. Buckling mode of rhombi-trihexagonal lattice compressed in x_2.

$$\begin{cases} M_{aa}+M_{ab}+M_{ac}+M_{ae}=0, \\ 2(M_{ba}+M_{bd})=0, \\ V_{ae}=0, \end{cases} \tag{192}$$

where the moments and transverse load are obtained using Eq. (178) and expressed as:

$$M_{aa}=\frac{E_sI}{\ell}s_{1aa}(1+c_{1aa})\theta_1, \tag{193a}$$

$$M_{ab}=\frac{E_sI}{\ell}(s_{ab}\theta_1-s_{ab}c_{ab}\theta_2), \tag{193b}$$

$$M_{ac}=\frac{E_sI}{\ell}(s_{ac}\theta_1+s_{ac}c_{ac}\theta_2), \tag{193c}$$

$$M_{ae}=\frac{E_sI}{\ell}\left(s_{ae}(1+c_{ae})\theta_1+\frac{\bar{s}_{ae}}{\ell}\Delta\right), \tag{193d}$$

$$M_{ba}=\frac{E_sI}{\ell}(s_{ab}c_{ab}\theta_1-s_{ab}\theta_2), \tag{193e}$$

$$M_{bd}=-\frac{E_sI}{\ell}(s_{bd}c_{bd}\theta_1+s_{bd}\theta_2), \tag{193f}$$

$$V_{ae}=\frac{E_sI}{\ell}\left(2\frac{\bar{s}_{ae}}{\ell}\theta_1+\frac{s^*_{ae}}{\ell^2}\Delta\right). \tag{193g}$$

The next steps are the same as those detailed in Appendix A.1. First, substitute (193) in (192) to form a linear system of equations and set the determinant of the coefficient matrix equal zero. Second, express the resulting equation as a function of λ_{ae} only (since this is the bar expected to buckle) using the following relations:

$$\begin{cases} \lambda^2_{1aa}=0.122\,\lambda^2_{ae}, \\ \lambda^2_{ab}=0.494\,\lambda^2_{ae}, \\ \lambda^2_{ac}=\lambda^2_{bd}=0.250\,\lambda^2_{ae}. \end{cases} \tag{194}$$

Solving the resultant expression returns $\lambda_{ae}=2.736$. Therefore, the end constraint factor for a rhombi-trihexagonal lattice compressed in x_2 is:

$$n=\frac{\lambda_{ae}}{\pi}=0.871. \tag{195}$$

A.3. Truncated-square lattice

A truncated-square tessellation is anticipated to buckle in a periodic swaying mode as shown in Fig. 14 when compressed in x_2. The analysis below is for compression in x_2, but, due to symmetry, the result is exactly the same when the lattice in compressed in x_1. The buckling shape in Fig. 14 is characterised by two rotations, θ_1 and θ_2, and two transverse displacements, Δ_1 and Δ_2. Equilibrium of moments at vertices a and b, as well as the transverse loads in bars aa and bb return the following set of equations:

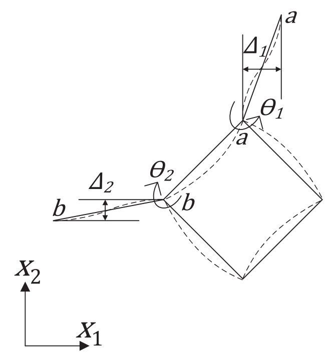

Fig. 14. Buckling mode of a truncated-square lattice compressed in x_2.

$$\begin{cases} M_{aa}+2M_{ab}=0, \\ M_{bb}+2M_{ba}=0, \\ V_{aa}=0, \\ V_{bb}=0, \end{cases} \tag{196}$$

where M_{ij} and V_{ij} are obtained using Eq. (178) and given by:

$$M_{aa}=\frac{E_sI}{\ell}\left(s_{aa}(1+c_{aa})\theta_1+\frac{\bar{s}_{aa}}{\ell}\Delta_1\right), \tag{197a}$$

$$M_{ab}=\frac{E_sI}{\ell}(s_{ab}\theta_1-s_{ab}c_{ab}\theta_2), \tag{197b}$$

$$M_{bb}=\frac{E_sI}{\ell}\left(-s_{bb}(1+c_{bb})\theta_2+\frac{\bar{s}_{bb}}{\ell}\Delta_2\right), \tag{197c}$$

$$M_{ba}=\frac{E_sI}{\ell}(s_{ab}c_{ab}\theta_1-s_{ab}\theta_2), \tag{197d}$$

$$V_{aa}=\frac{E_sI}{\ell}\left(2\frac{\bar{s}_{aa}}{\ell}\theta_1+\frac{s^*_{aa}}{\ell^2}\Delta_1\right), \tag{197e}$$

$$V_{bb}=\frac{E_sI}{\ell}\left(-2\frac{\bar{s}_{bb}}{\ell}\theta_2+\frac{s^*_{bb}}{\ell^2}\Delta_2\right). \tag{197f}$$

Note that bar bb does not carry any axial load and therefore, $s_{bb}=4$ and $c_{bb}=0.5$. Following the same procedure used for the two previous topologies, and the fact that $\lambda^2_{ab}=0.353\,\lambda^2_{aa}$, we find that $\lambda_{aa}=2.307$. Thus, the end constraint factor for a truncated-square lattice is:

$$n=\frac{\lambda_{aa}}{\pi}=0.734. \tag{198}$$

A.4. Truncated-trihexagonal lattice

A truncated-trihexagonal lattice may fail by elastic buckling when compressed in either x_1 or x_2. The periodic buckling shapes, for both loading directions, are given in Fig. 15. First, consider compression in x_1: the buckling shape is a swaying mode characterised by $\theta_1,\theta_2,\theta_3,\Delta_1$ and Δ_2. Equilibrium of moments at vertices a,c, and d, and transverse loads of bars aa and dd give the following set of equations:

$$\begin{cases} M_{aa}+M_{ab}+M_{ac}=0, \\ M_{ca}+M_{cd}+M_{ce}=0, \\ M_{dd}+M_{df}+M_{dc}=0, \\ V_{aa}=0, \\ V_{dd}=0, \end{cases} \tag{199}$$

where

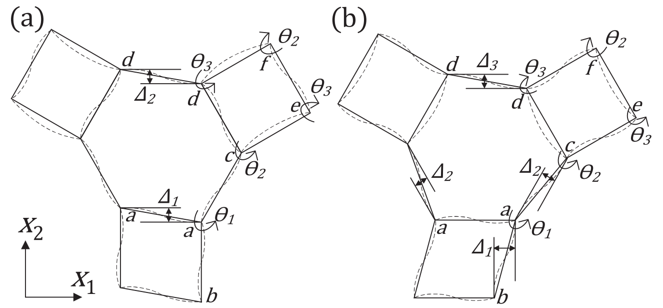

Fig. 15. Buckling modes of a truncated-trihexagonal lattice compressed in (a) x_1 and (b) x_2.

$$M_{aa} = \frac{E_sI}{\ell}\left(s_{aa}(1+c_{aa})\,\theta_1 + \frac{\bar{s}_{aa}}{\ell}\,\Delta_1\right), \tag{200a}$$

$$M_{ab} = \frac{E_sI}{\ell}s_{ab}(1+c_{ab})\,\theta_1, \tag{200b}$$

$$M_{ac} = \frac{E_sI}{\ell}(s_{ac}\,\theta_1 + s_{ac}c_{ac}\,\theta_2), \tag{200c}$$

$$M_{ca} = \frac{E_sI}{\ell}(s_{ac}c_{ac}\,\theta_1 + s_{ac}\,\theta_2), \tag{200d}$$

$$M_{cd} = \frac{E_sI}{\ell}(s_{cd}\,\theta_2 + s_{cd}c_{cd}\,\theta_3), \tag{200e}$$

$$M_{ce} = \frac{E_sI}{\ell}(s_{ce}\,\theta_2 - s_{ce}c_{ce}\,\theta_3), \tag{200f}$$

$$M_{dd} = \frac{E_sI}{\ell}\left(s_{dd}(1+c_{dd})\,\theta_3 + \frac{\bar{s}_{dd}}{\ell}\,\Delta_3\right), \tag{200g}$$

$$M_{df} = \frac{E_sI}{\ell}(s_{df}\,\theta_3 - s_{df}c_{df}\,\theta_2), \tag{200h}$$

$$M_{dc} = \frac{E_sI}{\ell}(s_{cd}\,\theta_3 + s_{cd}c_{cd}\,\theta_2), \tag{200i}$$

$$V_{aa} = \frac{E_sI}{\ell}\left(2\,\frac{\bar{s}_{aa}}{\ell}\,\theta_1 + \frac{s^*_{aa}}{\ell^2}\Delta_1\right), \tag{200j}$$

$$V_{dd} = \frac{E_sI}{\ell}\left(2\,\frac{\bar{s}_{dd}}{\ell}\,\theta_3 + \frac{s^*_{dd}}{\ell^2}\Delta_2\right). \tag{200k}$$

Note that bar ab, does not carry any axial load and therefore, $s_{ab} = 4$ and $c_{ab} = 0.5$. Substituting Eq. (200) in (199), then setting the determinant of the coefficient matrix to zero, and making use of the following relations:

$$\begin{cases} \lambda_{aa}^2 = 0.150\,\lambda_{dd}^2, \\ \lambda_{ac}^2 = 0.075\,\lambda_{dd}^2, \\ \lambda_{cd}^2 = 0.210\,\lambda_{dd}^2, \\ \lambda_{ce}^2 = \lambda_{df}^2 = 0.500\,\lambda_{dd}^2, \end{cases} \tag{201}$$

returns an expression where λ_{dd} is the only unknown (bar dd is the bar expected to buckle for compression in x_1). Solving this expression numerically returns $\lambda_{dd} = 2.491$; therefore, the end constrain factor for a truncated-trihexagonal lattice compressed in x_1 is:

$$n = \frac{\lambda_{dd}}{\pi} = 0.793. \tag{202}$$

Next, consider a truncated-trihexagonal lattice compressed in x_2, see Fig. 15b. We have:

$$\begin{cases} M_{aa} + M_{ab} + M_{ac} = 0, \\ M_{ca} + M_{cd} + M_{ce} = 0, \\ M_{dd} + M_{df} + M_{dc} = 0, \\ V_{ab} = 0, \\ V_{ac} = \frac{E_sI}{5}\left(\frac{\lambda_{ac}}{\ell}\right)^2, \\ V_{dd} = 0, \end{cases} \tag{203}$$

where the moments and transverse forces are:

$$M_{aa} = \frac{E_sI}{\ell}s_{aa}(1+c_{aa})\,\theta_1, \tag{204a}$$

$$M_{ab} = \frac{E_sI}{\ell}\left(s_{ab}(1+c_{ab})\,\theta_1 + \frac{\bar{s}_{ab}}{\ell}\,\Delta_1\right), \tag{204b}$$

$$M_{ac} = \frac{E_sI}{\ell}\left(s_{ac}\,\theta_1 + s_{ac}c_{ac}\,\theta_2 + \frac{\bar{s}_{ac}}{\ell}\,\Delta_2\right), \tag{204c}$$

$$M_{ca} = \frac{E_sI}{\ell}\left(s_{ac}c_{ac}\,\theta_1 + s_{ac}\,\theta_2 + \frac{\bar{s}_{ac}}{\ell}\,\Delta_2\right), \tag{204d}$$

$$M_{cd} = \frac{E_sI}{\ell}(s_{cd}\,\theta_2 - s_{cd}c_{cd}\,\theta_3), \tag{204e}$$

$$M_{ce} = \frac{E_sI}{\ell}(s_{ce}\,\theta_2 + s_{ce}c_{ce}\,\theta_3), \tag{204f}$$

$$M_{dd} = \frac{E_sI}{\ell}\left(-s_{1dd}(1+c_{1dd})\,\theta_3 + \frac{\bar{s}_{1dd}}{\ell}\,\Delta_3\right), \tag{204g}$$

$$M_{df} = \frac{E_sI}{\ell}(-s_{df}\,\theta_3 - s_{df}c_{df}\,\theta_2), \tag{204h}$$

$$M_{dc} = \frac{E_sI}{\ell}(-s_{cd}\,\theta_3 + s_{cd}c_{cd}\,\theta_2), \tag{204i}$$

$$V_{ab} = \frac{E_sI}{\ell}\left(2\,\frac{\bar{s}_{ab}}{\ell}\,\theta_1 + \frac{s^*_{ab}}{\ell^2}\Delta_1\right), \tag{204j}$$

$$V_{ac} = \frac{E_sI}{\ell}\left(\frac{\bar{s}_{ac}}{\ell}\,(\theta_1+\theta_2) + \frac{s^*_{ac}}{\ell^2}\Delta_2\right), \tag{204k}$$

$$V_{dd} = \frac{E_sI}{\ell}\left(-2\,\frac{\bar{s}_{1dd}}{\ell}\,\theta_3 + \frac{s^*_{1dd}}{\ell^2}\Delta_3\right). \tag{204l}$$

For compression in x_2, bar ab is expected to buckle and the proportionality between axial forces implies that:

$$\begin{cases} \lambda_{aa}^2 = \lambda_{1dd}^2 = 0.341\,\lambda_{ab}^2, \\ \lambda_{ac}^2 = 1.034\,\lambda_{ab}^2, \\ \lambda_{cd}^2 = 0.261\,\lambda_{ab}^2, \\ \lambda_{ce}^2 = \lambda_{df}^2 = 0.250\,\lambda_{ab}^2, \end{cases} \tag{205}$$

Following the same procedure as in x_1, we find that $\lambda_{ab} = 2.143$ and the end constrain factor for compression in x_2 is:

$$n = \frac{\lambda_{ab}}{\pi} = 0.682. \tag{206}$$

A.5. Snub-square lattice

A snub-square lattice may fail by elastic buckling when compressed in x_1 or x_2. The analysis is the same for both loading directions due to symmetry and therefore, we will consider only compression in x_2 here. The periodic buckling mode for this loading scenario is shown in Fig. 16. Equilibrium of moments at vertex a requires that:

$$2(M_{ab} + M_{ad}) + M_{ac} = 0, \tag{207}$$

where the moments are:

$$M_{ab} = \frac{E_sI}{\ell}(-4)\theta \tag{208a}$$

$$M_{ad} = \frac{E_sI}{\ell}(-s_{ad})\theta \tag{208b}$$

$$M_{ac} = \frac{E_sI}{\ell}(s_{ac}(c_{ac}-1))\theta. \tag{208c}$$

Note that the above results are based on the internal loads derived by Their and St-Pierre [32]. They showed that $N_{ab} = 0$, whereas bars ad and ac are both in compression with $N_{ad} = 0.577N_{ac}$. Substituting these moments in Eq. (207) gives:

$$s_{ac}(c_{ac}-1) - 2s_{ad} - 8 = 0, \tag{209}$$

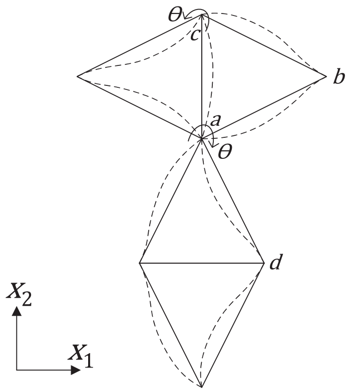

Fig. 16. Buckling mode of a snub-square lattice compressed in x_2.

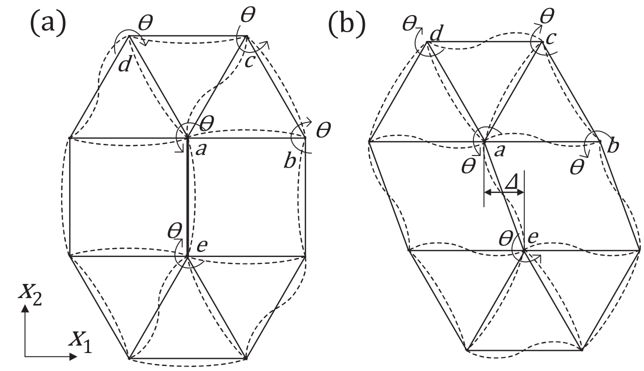

Fig. 17. Buckling modes of an elongated-triangular lattice compressed in (a) x_1 and (b) x_2.

and, with the definitions in Eq. (181) and (182), this becomes:

$$\frac{\lambda_{ac}(\lambda_{ac} - 2\sin\lambda_{ac} + \lambda_{ac}\cos\lambda_{ac})}{2 - 2\cos\lambda_{ac} - \lambda_{ac}\sin\lambda_{ac}} - \frac{2\lambda_{ad}(\sin\lambda_{ad} - \lambda_{ad}\cos\lambda_{ad})}{2 - 2\cos\lambda_{ad} - \lambda_{ad}\sin\lambda_{ad}} - 8 = 0. \tag{210}$$

This equation can be expressed as a function of λ_{ac} only since $\lambda_{ad}^2 = 0.577\lambda_{ac}^2$. Doing that and solving numerically returns $\lambda_{ac} = 5.319$ and consequently, the end constraint factor for a snub-square lattice is:

$$n = \frac{\lambda_{ac}}{\pi} = 1.693. \tag{211}$$

A.6. Elongated-triangular lattice

An elongated-triangular lattice is anticipated to buckle in the pattern shown Fig. 17a when compressed in x_1. Equilibrium of moments at vertex a requires that:

$$2M_{ab} + M_{ac} + M_{ad} + M_{ae} = 0, \tag{212}$$

where

$$M_{ab} = \frac{E_s I}{\ell}(s_{ab} - s_{ab}c_{ab})\theta, \tag{213a}$$

$$M_{ac} = \frac{E_s I}{\ell}(4 + 2)\theta, \tag{213b}$$

$$M_{ad} = M_{ae} = \frac{E_s I}{\ell}(4 - 2)\theta. \tag{213c}$$

The above expressions are based on the fact that bar ab is in compression whereas bars ac, ad and ae do not carry any axial load for compression in x_1, see Eq. (141). Substituting Eq. (213) in (212) gives:

$$s_{ab}(1 - c_{ab}) + 5 = 0 \Rightarrow \frac{\lambda_{ab}(\lambda_{ab} - 2\sin\lambda_{ab} + \lambda_{ab}\cos\lambda_{ab})}{2\cos\lambda_{ab} + \lambda_{ab}\sin\lambda_{ab} - 2} + 5 = 0. \tag{214}$$

Solving this expression numerically returns $\lambda_{ab} = 4.761$ and consequently, the end constraint factor for compression in x_1 is:

$$n = \frac{\lambda_{ab}}{\pi} = 1.515. \tag{215}$$

Otherwise, an elongated-triangular lattice is expected to buckle in the swaying pattern shown in Fig. 17b when compressed in x_2. The vertical bar ae has a transverse displacement Δ, and all vertices have the same rotation θ. Again, the sum of moments should be zero at vertex a and therefore, Eq. (212) remains valid, but for this loading direction the moments are:

$$M_{ab} = \frac{E_s I}{\ell}(s_{1ab} + s_{1ab}c_{1ab})\theta, \tag{216a}$$

$$M_{ac} = M_{ad} = \frac{E_s I}{\ell}(s_{ac} - s_{ac}c_{ac})\theta, \tag{216b}$$

$$M_{ae} = \frac{E_s I}{\ell}\left((s_{ae} + s_{ae}c_{ae})\theta - \frac{\bar{s}_{ae}}{\ell}\Delta\right), \tag{216c}$$

where the subscript 1 appear in M_{ab} because this bar is under tension. In addition, $M_{ac} = M_{ad}$ since they have the same rotations and carry the same axial compressive load, see Eq. (133). Substituting Eq. (216) in (212) yields:

$$(2s_{1ab}(1 + c_{1ab}) + 2s_{ac}(1 - c_{ac}) + s_{ae}(1 + c_{ae}))\theta - \frac{\bar{s}_{ae}}{\ell}\Delta = 0, \tag{217}$$

and the transverse force in bar ae gives:

$$V_{ae} = \frac{E_s I}{\ell}\left(\frac{2\bar{s}_{ae}}{\ell}\theta - \frac{s^*_{ae}}{\ell^2}\Delta\right) = 0. \tag{218}$$

The last two expressions form a system of linear equations and setting the determinant of the coefficient matrix equal to zero, along with the fact that the proportionality between internal axial loads (see Eq. (133)) implies that:

$$\begin{cases} \lambda_{1ab}^2 = 0.144\lambda_{ae}^2, \\ \lambda_{ac}^2 = 0.577\lambda_{ae}^2, \end{cases} \tag{219}$$

we obtain a long expression where λ_{ae} is the only unknown. Solving this expression numerically returns $\lambda_{ae} = 2.767$ and consequently, the end constraint factor n for compression in x_2 is:

$$n = \frac{\lambda_{ae}}{\pi} = 0.881. \tag{220}$$

A.7. Snub-trihexagonal lattice

The snub-trihexagonal lattice is stretching-dominated and may fail by elastic buckling when loaded in compression or shear. First, consider the lattice under uniaxial compression in the x_1 direction. The periodic buckling shape for this loading scenario is shown in Fig. 18a, and equilibrium of moments at vertices b, c, and d return:

$$M_{bc} + M_{ba} + M_{bl} + M_{bk} + M_{bj} = 0, \tag{221a}$$

$$M_{cb} + M_{cj} + M_{ci} + M_{ch} + M_{cd} = 0, \tag{221b}$$

$$M_{dc} + M_{de} + M_{df} + M_{dg} + M_{dh} = 0, \tag{221c}$$

respectively. Using Eq. (178) to express each moment as a function of the rotations, the above three equations become:

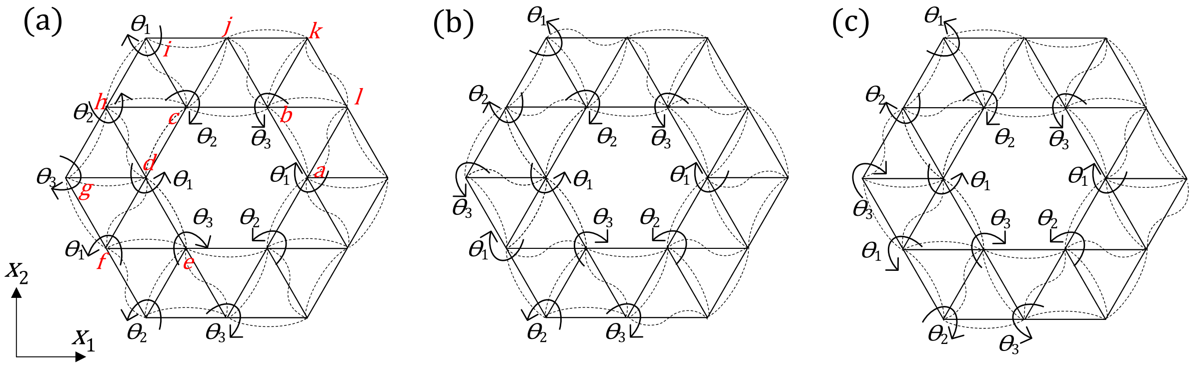

Fig. 18. Buckling modes of a snub-trihexagonal lattice (a) compressed in x_1, (b) compressed in x_2, and (c) in shear.

$$\begin{aligned} s_{bc}(\theta_3 - c_{bc}\theta_2) + s_{ab}(\theta_3 - c_{ab}\theta_1) + \\ s_{bl}(\theta_3 - c_{bl}\theta_1) + s_{bk}(\theta_3 - c_{bk}\theta_2) + \\ s_{bj}(\theta_3 + c_{bj}\theta_3) = 0, \end{aligned} \tag{222a}$$

$$\begin{aligned} s_{bc}(-\theta_2 + c_{bc}\theta_3) + s_{cj}(-\theta_2 + c_{cj}\theta_3) + \\ s_{ci}(-\theta_2 - c_{ci}\theta_1) + s_{ch}(-\theta_2 + c_{ch}\theta_2) + \\ s_{cd}(-\theta_2 + c_{cd}\theta_1) = 0, \end{aligned} \tag{222b}$$

$$\begin{aligned} s_{cd}(\theta_1 - c_{cd}\theta_2) + s_{de}(\theta_1 - c_{de}\theta_3) + \\ s_{1df}(\theta_1 + c_{1df}\theta_1) + s_{dg}(\theta_1 - c_{dg}\theta_3) + \\ s_{1dh}(\theta_1 + c_{1dh}\theta_2) = 0, \end{aligned} \tag{222c}$$

respectively. Note that $s_{cd} = s_{bj} = 4$ and $c_{cd} = c_{bj} = 0.5$ since these bars are not carrying any axial load, see Eq. (166). The three expressions above form a linear system of equations $\boldsymbol{A}\theta = \boldsymbol{0}$, where the determinant of $\boldsymbol{A}$ should be zero to ensure that a non-trivial solution exists. Setting $\det(\boldsymbol{A}) = 0$ returns a lengthy expression with coefficients s_{mn} and c_{mn}, which can be expressed as a function of λ_{mn} using Eqs. (181)–(185). Next, we use the internal loads given in Eq. (166) to express each term as a function of λ_{ch} (this is the bar expected to buckle for compression in x_1) and this yields:

$$\begin{cases} \lambda_{bc}^2 = 0.75\lambda_{ch}^2, \\ \lambda_{ab}^2 = \lambda_{bk}^2 = \lambda_{cj}^2 = \lambda_{ci}^2 = \lambda_{de}^2 = \lambda_{1dh}^2 = 0.25\lambda_{ch}^2, \\ \lambda_{bl}^2 = \lambda_{1df}^2 = \lambda_{dg}^2 = 0.5\lambda_{ch}^2. \end{cases} \tag{223}$$

This returns a lengthy expression where λ_{ch} is the only unknown, and solving numerically yields $\lambda_{ch} = 5.219$. Therefore, the end constraint factor n for compression in x_1 is:

$$n = \frac{\lambda_{ch}}{\pi} = 1.661. \tag{224}$$

Next, consider the snub-trihexagonal lattice compressed in the x_2 direction. The anticipated buckling pattern for this case is shown in Fig. 18b. The three expressions in Eq. (221) are still valid, but the moments are different for this loading scenario, which gives:

$$\begin{aligned} s_{1bc}(\theta_3 - c_{1bc}\theta_2) + s_{ab}(\theta_3 - c_{ab}\theta_1) + \\ s_{bl}(\theta_3 + c_{bl}\theta_1) + s_{bk}(\theta_3 - c_{bk}\theta_2) + \\ s_{bj}(\theta_3 + c_{bj}\theta_3) = 0, \end{aligned} \tag{225a}$$

$$\begin{aligned} s_{1bc}(-\theta_2 + c_{1bc}\theta_3) + s_{cj}(-\theta_2 + c_{cj}\theta_3) + \\ s_{ci}(-\theta_2 + c_{ci}\theta_1) + s_{1ch}(-\theta_2 - c_{1ch}\theta_2) + \\ s_{cd}(-\theta_2 + c_{cd}\theta_1) = 0, \end{aligned} \tag{225b}$$

$$\begin{aligned} s_{cd}(\theta_1 - c_{cd}\theta_2) + s_{de}(\theta_1 - c_{de}\theta_3) + \\ s_{df}(\theta_1 - c_{df}\theta_1) + s_{1dg}(\theta_1 + c_{1dg}\theta_3) + \\ s_{dh}(\theta_1 - c_{dh}\theta_2) = 0. \end{aligned} \tag{225c}$$

Otherwise, the internal loads given in Eq. (159) implies that:

$$\begin{cases} \lambda_{1bc}^2 = \lambda_{bk}^2 = \lambda_{cj}^2 = 0.1\lambda_{df}^2, \\ \lambda_{ab}^2 = \lambda_{de}^2 = 0.5\lambda_{df}^2, \\ \lambda_{bl}^2 = \lambda_{1dg}^2 = 0.2\lambda_{df}^2, \\ \lambda_{bj}^2 = 0.4\lambda_{df}^2, \\ \lambda_{ci}^2 = \lambda_{dh}^2 = 0.7\lambda_{df}^2, \\ \lambda_{1ch}^2 = \lambda_{cd}^2 = 0.8\lambda_{df}^2. \end{cases} \tag{226}$$

Following the same procedure detailed above (for compression in x_1), we obtain a constitutive equation as a function of λ_{df} only, since this is the most loaded bar and the one expected to buckle. Solving this expression returns $\lambda_{df} = 4.841$, and therefore, the end constraint factor for compression in x_2 is:

$$n = \frac{\lambda_{df}}{\pi} = 1.541. \tag{227}$$

Finally, a snub-trihexagonal lattice can also buckle elastically under shear according to the pattern shown in Fig. 18c. For this buckling mode, the three expressions in Eq. (221) become:

$$\begin{aligned} s_{1bc}(\theta_3 - c_{1bc}\theta_2) + s_{ab}(\theta_3 - c_{ab}\theta_1) + \\ s_{bl}(\theta_3 - c_{bl}\theta_1) + s_{bk}(\theta_3 + c_{bk}\theta_2) + \\ s_{bj}(\theta_3 - c_{bj}\theta_3) = 0, \end{aligned} \tag{228a}$$

$$\begin{aligned} s_{1bc}(-\theta_2 + c_{1bc}\theta_3) + s_{1cj}(-\theta_2 - c_{1cj}\theta_3) + \\ s_{ci}(-\theta_2 + c_{ci}\theta_1) + s_{1ch}(-\theta_2 - c_{1ch}\theta_2) + \\ s_{1cd}(-\theta_2 + c_{1cd}\theta_1) = 0, \end{aligned} \tag{228b}$$

$$\begin{aligned} s_{1cd}(\theta_1 - c_{1cd}\theta_2) + s_{de}(\theta_1 - c_{de}\theta_3) + \\ s_{1df}(\theta_1 + c_{1df}\theta_1) + s_{dg}(\theta_1 - c_{dg}\theta_3) + \\ s_{dh}(\theta_1 - c_{dh}\theta_2) = 0. \end{aligned} \tag{228c}$$

In addition, the internal loads in Eq. (172) implies that:

$$\begin{cases} \lambda_{1bc}^2 = \lambda_{ci}^2 = \lambda_{dh}^2 = 0.167\lambda_{bj}^2, \\ \lambda_{ab}^2 = \lambda_{bk}^2 = \lambda_{cj}^2 = \lambda_{de}^2 = 0.5\lambda_{bj}^2, \\ \lambda_{bl}^2 = \lambda_{1ch}^2 = \lambda_{1cd}^2 = \lambda_{dg}^2 = 0.333\lambda_{bj}^2, \\ \lambda_{1df}^2 = 0.667\lambda_{bj}^2. \end{cases} \tag{229}$$

Following the same procedure employed for compression, we obtain a constitutive equation as a function of λ_{bj} and find $\lambda_{bj} = 5.469$. Consequently, the end constraint factor in shear is:

$$n = \frac{\lambda_{bj}}{\pi} = 1.741. \tag{230}$$

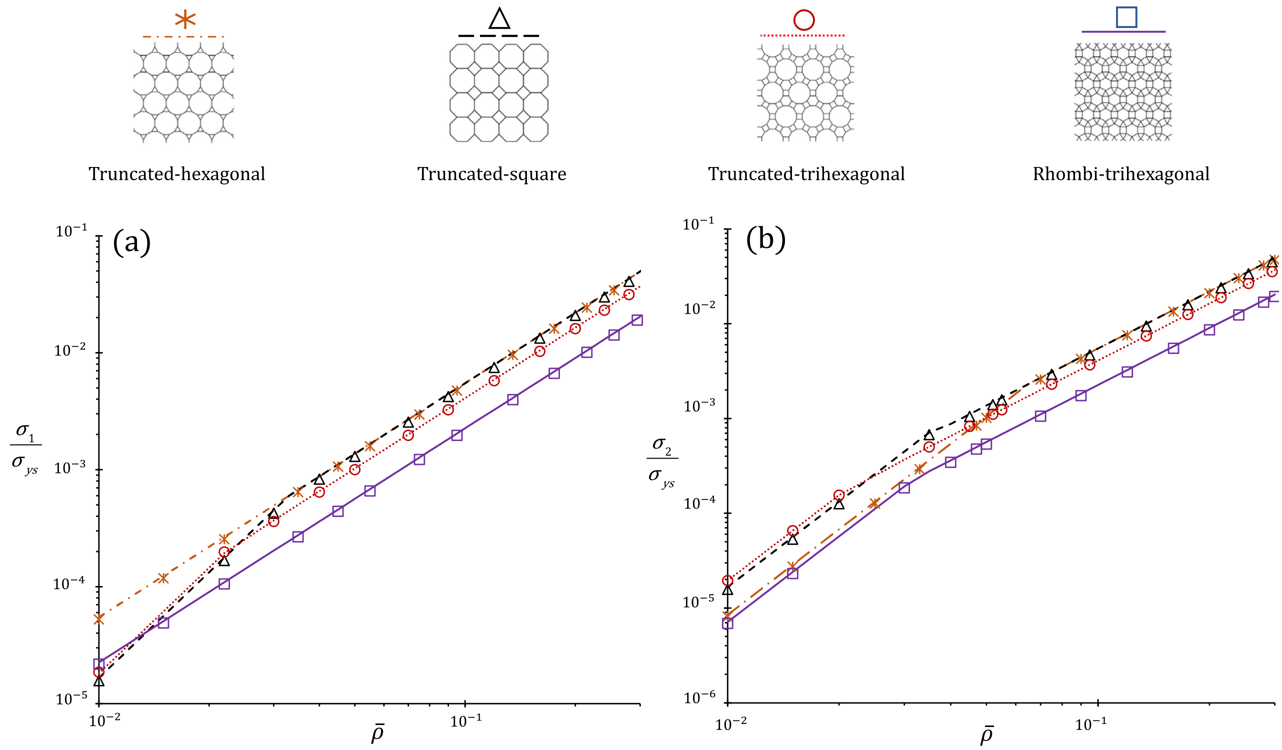

Fig. 19. Comparison between analytical (lines) and FE (symbols) results for the normalised compressive strength of bending-dominated semi-regular lattices: (a) σ_1, and (b) σ_2, both plotted as a function of relative density $\bar{\rho}$. The properties of the parent material are $E_s = 4\,\text{GPa}$ and $\sigma_{ys} = 40\,\text{MPa}$.

Appendix B. Elastic buckling strength of bending-dominated topologies

Additional FE simulations were performed to capture the elastic buckling strength of the four bending-dominated semi-regular lattices. These FE predictions were conducted using the methodology described in Section 3, except that the properties of the parent material were changed to $E_s = 4\,\text{GPa}$ and $\sigma_{ys} = 40\,\text{MPa}$. These material properties are representative of many polymers.

The compressive strengths in both directions, σ_1 and σ_2, are plotted as a function of $\bar{\rho}$ in Fig. 19. In each plot, analytical predictions (lines) are compared to FE results (symbols) for all four bending-dominated semi-regular topologies. The failure mode switches from plastic collapse (at high values of relative density) to elastic buckling (at low values of $\bar{\rho}$). There are, however, two exceptions: the truncated-hexagonal and rhombi-trihexagonal lattices do not fail by elastic buckling when compressed in x_1, which is in-line with our analytical model (see Sections 2.1.1 and 2.2.1). In general, there is an excellent agreement between analytical and FE results; therefore, we conclude that our analytical expressions for the elastic buckling strength of bending-dominated lattices are verified.

Appendix C. Supplementary material

Supplementary data associated with this article can be found, in the online version, at https://doi.org/10.1016/j.matdes.2021.110324.

References

[1] M. Kadic, G.W. Milton, M. van Hecke, M. Wegener, 3D metamaterials, Nat. Rev. Phys. 1 (2019) 198–210.

[2] J.U. Surjadi, L. Gao, H. Du, X. Li, X. Xiong, N.X. Fang, Y. Lu, Mechanical metamaterials and their engineering applications, Adv. Eng. Mater. 21 (2019) 1800864.

[3] J. Berger, H. Wadley, R. McMeeking, Mechanical metamaterials at the theoretical limit of isotropic elastic stiffness, Nature 543 (2017) 533–537.

[4] T. Tancogne-Dejean, M. Diamantopoulou, M.B. Gorji, C. Bonatti, D. Mohr, 3D plate-lattices: An emerging class of low-density metamaterial exhibiting optimal isotropic stiffness, Adv. Mater. 30 (2018) 1803334.

[5] J.N. Heidenreich, M.B. Gorji, T. Tancogne-Dejean, D. Mohr, Design of isotropic porous plates for use in hierarchical plate-lattices, Mater. Des. 212 (2021) 110218.

[6] Y. Liu, L. St-Pierre, N.A. Fleck, V.S. Deshpande, A. Srivastava, High fracture toughness micro-architectured materials, J. Mech. Phys. Solids 143 (2020) 104060.

[7] K.M. Conway, C. Kunka, B.C. White, G.J. Pataky, B.L. Boyce, Increasing fracture toughness via architected porosity, Mater. Des. 205 (2021) 109696.

[8] S. Yin, W. Guo, H. Wang, W. Huang, R. Yang, Z. Hu, D. Chen, J. Xu, R.O. Ritchie, Strong and tough bioinspired additive-manufactured dual-phase mechanical metamaterial composites, J. Mech. Phys. Solids 149 (2021) 104341.

[9] L. Bai, Y. Xu, X. Chen, L. Xin, J. Zhang, K. Li, Y. Sun, Improved mechanical properties and energy absorption of Ti6Al4V laser powder bed fusion lattice structures using curving lattice struts, Mater. Des. 211 (2021) 110140.

[10] P. Wang, F. Yang, D. Ru, B. Zheng, H. Fan, Additive-manufactured hierarchical multi-circular lattice structures for energy absorption application, Mater. Des. 210 (2021) 110116.

[11] Q. Wang, Z. Yang, Z. Lu, X. Li, Mechanical responses of 3d cross-chiral auxetic materials under uniaxial compression, Mater. Des. 186 (2020) 108226.

[12] H. Ebrahimi, D. Mousanezhad, H. Nayeb-Hashemi, J. Norato, A. Vaziri, 3D cellular metamaterials with planar anti-chiral topology, Mater. Des. 145 (2018) 226–231.

[13] D. De Tommasi, G.C. Marano, G. Puglisi, F. Trentadue, Morphological optimization of tensegrity-type metamaterials, Compos. B Eng. 115 (2017) 182–187.

[14] J. Bauer, J.A. Kraus, C. Crook, J.J. Rimoli, L. Valdevit, Tensegrity metamaterials: toward failure-resistant engineering systems through delocalized deformation, Adv. Mater. 33 (2021) 2005647.

[15] M. Kadic, T. Bückmann, N. Stenger, On the practicability of pentamode mechanical metamaterials, Appl. Phys. Lett. 100 (2012) 191901.

[16] A.A. Sabouni-Zawadzka, Extreme mechanical properties of regular tensegrity unit cells in 3D lattice metamaterials, Materials 13 (2020) 4845.

[17] N.A. Fleck, V.S. Deshpande, M.F. Ashby, Micro-architectured materials: past, present and future, Proc. R. Soc. A 466 (2010) 2495–2516.

[18] R. Williams, The geometrical foundation of natural structure: A source book of design, Dover, New York, 1979.

[19] M.F. Ashby, The properties of foams and lattices, Philos. Trans. R. Soc. A 364 (2006) 15–30.

[20] V.S. Deshpande, M.F. Ashby, N.A. Fleck, Foam topology: bending versus stretching dominated architectures, Acta Mater. 49 (2001) 1035–1040.

[21] L.J. Gibson, M.F. Ashby, Cellular solids: structure & properties, 2 ed., Cambridge University Press, 1997.

[22] S. Torquato, L.V. Gibiansky, M.J. Silva, L.J. Gibson, Effective mechanical and transport properties of cellular solids, Int. J. Mech. Sci. 40 (1998) 71–82.
[23] A.J. Wang, D.L. McDowell, In-plane stiffness and yield strength of periodic metal honeycombs, J. Eng. Mater. Technol. 126 (2004) 137–156.
[24] F. Côté, V.S. Deshpande, N.A. Fleck, A.G. Evans, The compressive and shear responses of corrugated and diamond lattice materials, Int. J. Solids Struct. 43 (2006) 6220–6242.
[25] H. Fan, F. Jin, D. Fang, Uniaxial local buckling strength of periodic lattice composites, Mater. Des. 30 (2009) 4136–4145.
[26] H.C. Tankasala, V.S. Deshpande, N.A. Fleck, Tensile response of elastoplastic lattices at finite strain, J. Mech. Phys. Solids 109 (2017) 307–330.
[27] H. Gu, M. Pavier, A. Shterenlikht, Experimental study of modulus, strength and toughness of 2D triangular lattices, Int. J. Solids Struct. 152–153 (2018) 207–216.
[28] S. Hyun, S. Torquato, Optimal and manufacturable two-dimensional, Kagomé-like cellular solids, J. Mater. Res. 17 (2002) 137–144.
[29] N.A. Fleck, X.M. Qiu, The damage tolerance of elastic-brittle, two-dimensional isotropic lattices, J. Mech. Phys. Solids 55 (2007) 562–588.
[30] R.G. Hutchinson, N. Wicks, A.G. Evans, N.A. Fleck, J.W. Hutchinson, Kagome plate structures for actuation, Int. J. Solids Struct. 40 (2003) 6969–6980.
[31] D.D. Symons, R.G. Hutchinson, N.A. Fleck, Actuation of the Kagome Double-Layer Grid. Part 1: Prediction of performance of the perfect structure, J. Mech. Phys. Solids 53 (2005) 1855–1874.
[32] T. Their, L. St-Pierre, Stiffness and strength of a semi-regular lattice, Raken. Mek. 50 (2017) 137–140.
[33] M.S.A. Elsayed, D. Pasini, Analysis of the elastostatic specific stiffness of 2D stretching-dominated lattice materials, Mech. Mater. 42 (2010) 709–725.
[34] T.N. Pronk, C. Ayas, C. Tekõglu, A quest for 2D lattice materials for actuation, J. Mech. Phys. Solids 105 (2017) 199–216.
[35] S.P. Timoshenko, J.M. Gere, Theory of elastic stability, 2 ed., McGraw-Hill, New York, 1961.
[36] Z.P. Bažant, L. Cedolin, Stability of structures: elastic, inelastic, fracture and damage theories, World Scientific, 2010.
[37] R.M. Christensen, Sufficient symmetry conditions for isotropy of the elastic moduli tensor, J. Appl. Mech. 54 (1987) 772–777.